Engineering Structures 315 (2024) 118348

Contents lists available at ScienceDirect

Engineering Structures

journal homepage: www.elsevier.com/locate/engstruct

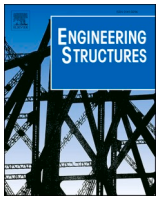

Development of multi-directional real-time hybrid simulation for tall buildings subject to multi-natural hazards

Safwan Al-Subaihawi [a,1], James Ricles [a,*,2], Spencer Quiel [a], Thomas Marullo [b]

[a] Department of Civil and Environmental Eng, Lehigh Univ, 117 ATLSS Dr, Bethlehem, PA 18015, United States
[b] ATLSS Eng Research Center, Lehigh Univ, 117 ATLSS Dr, Bethlehem, PA 18015, United States

ARTICLE INFO

Keywords:
Damped outrigger system
3D nonlinear model
Large-scale multi-directional real-time hybrid simulation
Real-time online model updating
Nonlinear viscous dampers
Tall buildings
Multi-natural hazards
Adaptive servo-hydraulic actuator control
RTHS half-power testing method

ABSTRACT

Real-time hybrid simulation (RTHS) divides a structural system into analytical and experimental substructures that are coupled through their common degrees of freedom. This paper introduces a framework to enable RTHS to be performed on 3D nonlinear models of tall buildings with rate dependent nonlinear response modification devices, where the structure is subjected to multi-directional wind and earthquake natural hazards. A 40-story tall building prototype with damped outriggers is selected as a case study. The analytical substructure for the RTHS consists of a 3-D nonlinear model of the structure, where each member in the building is discretely modeled in conjunction with the use of a super element. The experimental substructure for the RTHS consists of a full-scale rate-dependent nonlinear viscous damper that is physically tested in the lab, with the remaining dampers in the outrigger system modeled analytically. The analytically modeled dampers use a stable explicit non-iterative element with an online model updating algorithm, by which the covariance matrix of the damper model's state variables does not become ill-conditioned. The damper model parameters can thereby be updated in real-time using measured data from the experimental substructure. The explicit MKR-α method is optimized and used in conjunction with the super element to efficiently integrate the condensed equations of motion of a large complex model having more than 1000 nonlinear elements, thus enabling multi-axis earthquake and wind hybrid nonlinear simulations to be performed in real-time. An adaptive servo-hydraulic actuator control scheme is used to enable precise real-time actuator displacements in the experimental substructure to be achieved that match the target displacements during a RTHS. The IT real-time architecture for integrating the components of the framework is described. To assess the framework, 3D RTHS of the 40-story structure were performed involving multi-axis translational and torsional response to multi-directional earthquake and wind natural hazards. The RTHS technique was applied to perform half-power tests to experimentally determine the amount of supplemental damping provided by the damped outrigger system for translational and torsional modes of vibration of the building. The results from the study presented herein demonstrate that RTHS can be applied to large nonlinear large structural systems involving multi-axis response to multi-directional excitation.

1. Introduction

Hybrid simulation divides a structural system into analytical and experimental substructures which are coupled through their common degrees of freedoms [1–3]. Real-time hybrid simulation (RTHS) is performed in real time and is needed to accommodate the presence of load-rate dependent experimental substructures as components within the larger analytically modeled system [2]. The analytical substructure for a RTHS is comprised of components of the system that can be accurately modeled numerically, while the remaining components of the system that are difficult to model analytically are modeled physically via an experimental substructure in the laboratory. This paper extends RTHS to simulations of a 40-story tall building with a damped outrigger system that is subjected to multi-directional wind and earthquake natural hazards.

The damped outrigger system presented in this paper consists of nonlinear viscous dampers inserted between the ends of an outrigger truss and the adjacent perimeter columns of a building. Tall buildings

* Corresponding author.
E-mail address: jmr5@lehigh.edu (J. Ricles).
[1] ORCID: 0000-0002-7876-5738
[2] ORCID: 0000-0002-1545-5898

https://doi.org/10.1016/j.engstruct.2024.118348
Received 24 August 2023; Received in revised form 23 May 2024; Accepted 1 June 2024
Available online 20 June 2024
0141-0296/© 2024 Elsevier Ltd. All rights are reserved, including those for text and data mining, AI training, and similar technologies.

are known to have a minimal amount of inherent damping with a damping ratio of less than 1 %, particularly in structures that are taller than 250 m [4]. Smith and Willford [5] proposed damped outrigger systems to increase the damping of the building and improve its response to natural hazards. Buildings are subjected to wind load effects from all sides, where the differential pressure acting around the circumference of the structure will cause combined translational and story twist, which both contribute to floor accelerations. These accelerations are increased at the perimeter of the structure's floor plan, where the effects of angular accelerations have their greatest effect. Three-dimensional analytical models are needed to capture this effect. Seismic torsional loading arising from an eccentricity between the mass and center of rigidity is also a scenario where two-dimensional analytical models fail to capture the realistic response of a building.

Numerous analytical studies have been previously conducted to investigate the behavior of a damped outrigger system, such as those by Fang et al. [6]; Tan et al. [7]; Nagarajaiah et al. [8]; Wang et al. [9]; Xing et al. [10]; and Malik and Kolay [11]. In particular, the studies by Fang et al. [6], Tan et al. [7], Xing et al. [10], and Malik and Kolay [11] showed that the amount of supplemental damping achieved from a damped outrigger system is dependent on both the location of the outriggers and the damping constant of the dampers. Wang et al. [9] demonstrated the ability of a damped outrigger system to suppress cross-wind vibrations in tall buildings and the need to stiffen the perimeter columns that are in the load path of the dampers. Nagarajaiah et al. [8] placed negative stiffness response modification devices between an outrigger truss and perimeter columns to increase the deformation in response modification devices placed in the outrigger to dissipate larger amounts of energy as the system responds to external excitations. Such an arrangement was shown by Nagarajaiah et al. [8] to suppress wind induced floor accelerations. These studies used either a planar finite element model or other analytical models which do not account for the effects of multi-axis loading.

Many of the previous studies that have used RTHS have involved a planar structure, including those that examine tall buildings with nonlinear viscous dampers under wind and earthquake natural hazards [12,13] as well as the seismic performance of low-rise reinforced concrete and steel frame buildings with nonlinear viscous dampers [14,15] and elastomeric dampers [16,17]. Asai et al. [18] performed RTHS on a planar model of a 60-story building to experimentally verify the efficacy of smart outrigger MR-based damping systems for enhancing the seismic performance of high-rise buildings. There have been numerous developments to enable RTHS to be used for multi-axis response of structural systems. Prior studies include that by Fermandois and Spencer [19], who formulated a real-time feedback-feedforward model-based controller for multiple actuators in multi-axis RTHS. Najafi et al. [20] developed a framework with tracking compensation to enhance the controller stability when testing stiff specimens. These studies focused primarily on multi-axis loading where there was a strong coupling effect between multiple actuators in the experimental substructure. Najafi and Spencer [21] performed three-dimensional (3D) RTHS to investigate the 3D seismic behavior of a bridge structure. The study involved using a linear elastic analytical substructure, where the authors stated that their use of a linear elastic analytical substructure was based on the challenge of developing a 3D inelastic model that could accurately model the superstructure of the bridge system. While the results of their study provided new knowledge and extensions of RTHS to bridge structures subjected to multi-directional loading, the approach is not suitable for applications to tall buildings, in which many more DOFs exist and inelastic multi-axis structural response can occur during an earthquake.

The presence of a large number of structural degrees of freedom in the equations of motion and the state determination of the elements of the analytical substructure during a RTHS of a tall building can pose a computational bottleneck, in which the calculations for each time step in the integration procedure cannot be completed within the required time step. An additional challenge exists when there are many rate-dependent response modification devices throughout the structure and only a few of these devices are available to create physical models via an experimental substructure. In this situation, online model updating of the parameters of the model is often performed using experimental data from the experimental substructure [12,22–24]. In a tall building, the multi-directional loading can engage multiple vibration modes in the structure's response, resulting in different response characteristics for dampers whose response are not in phase and of different amplitude due to their varied locations throughout the structure. This can affect the accuracy of online model updating to predict the numerically modeled dampers with updated model parameters. Specifically, these updates are based on data from an experimental substructure that is not in phase and has a different amplitude than the dampers being modeled in the analytical substructure.

This paper presents the development, implementation, and assessment of a RTHS framework that overcomes the current barriers to using 3D multi-axis RTHS to investigate the nonlinear response of tall buildings subjected to multi-natural hazards. The 40-story building selected for the study has damped outriggers and is assumed to be located in Los Angeles, California. A 3D RTHS nonlinear analytical substructure model was developed to capture multi-directional translational and torsional effects, where the latter was noted previously as being caused by differential wind pressure acting around the circumference of the building and/or an eccentric mass with respect to the center of rigidity of a floor level. The equations of motion are integrated using an explicit dissipative integration algorithm that is unconditionally stable. The algorithm has been optimized and incorporates a super element to condense the number of degrees of freedom while retaining the nonlinear elements of the model, such that the integration can be completed in real-time for each time step.

The experimental substructure for the RTHS consisted of a full scale nonlinear viscous damper, with the other dampers in the building modeled analytically. The effects of multi-axis coupling of multiple actuators was therefore not present in the study. The parameters of the analytically modeled dampers are updated using an explicit real-time online model updating algorithm developed by the authors using measured data from the experimental substructure to ensure that the covariance matrix of the damper model's state variables will not become ill-conditioned. The potential for actuator delay and amplitude error exists during a RTHS. Consequently, an adaptive compensation actuator control law was used in the RTHS based on the Adaptive Time Series (ATS) compensator by Chae et al. [25]. High-rise structures subjected to multi-directional natural hazard loading can pose a challenge in actuator control since the structural response characteristics for each hazard type can differ (e.g., wind versus earthquake), which has an effect on the specimen-actuator interaction. The use of the ATS compensator for the multi-natural hazard RTHS of high-rise structures is assessed in this paper. In addition, a method was developed where the half-power testing method was performed using RTHS to experimentally quantify the amount of supplemental damping in the building that is generated by the viscous dampers placed in the outrigger system.

The results of the building's response from the 3D RTHS are presented to illustrate the response characteristics and the ability of the RTHS framework to capture true behavior of actual tall buildings subjected to multi-natural hazards. The accuracy of the newly developed online model updating algorithm along with the ATS compensator is evaluated for the multi-directionally loaded tall building, which experiences a multi-axis response due to wind and earthquake hazards. Finally, the results of the 3D RTHS half-power testing are presented and assessed.

2. Description of prototype building

The building used for the study is among the architypes for the California Tall Building Initiative [26] that was designed in accordance with the Tall Building Initiative Guidelines [27]. The Los Angeles

located structure has a height of 166 m with a 32.6 m by 51.7 m floor plan, see Fig. 1(a) and (b). The lateral load resisting system includes six buckling restrained braced frames (BRBFs) in both the north-south (N-S) and east-west (E-W) directions. The gravity load resisting system includes columns, beams, and light weight composite metal decking. The columns are comprised of square steel box columns with sizes ranging from 0.45 m to 1.4 m and filled with high strength concrete. They are fabricated from steel plates ranging from 38 mm to 76 mm in thickness. The beams are comprised of A992 steel wide flange sections. The columns and beams are designed to remain elastic when the buckling restrained braces (BRBs) yield. The BRBs have a strength ranging from 2045 kN to 3440 kN over the height of the building. The beam-to-column connections are shear connections that do not resist moment. The building includes six outrigger trusses located at the 20th, 30th, and 40th stories in the north-south direction. There are no connections between the floor diaphragm to the outrigger trusses to create a lateral load path in the E-W direction of the building to the outrigger trusses, and therefore the outrigger system only acts in the plane of the outriggers. The floor diaphragms of the building are constructed of composite floor slabs consisting of lightweight concrete cast on top of metal decking. The building has a basement of four story levels. Additional details regarding the building design can be found in Moehle et al. [26].

The building was designed by Moehle et al. [26] with the following performance objectives: 1) elastic behavior with no major BRB yielding and a maximum story drift of less than 0.5 % under the frequently occurring 43-year return period earthquake; 2) collapse prevention under the 2475-year return period Maximum Considered Earthquake (MCE) with a maximum story drift of less than 3 %; and, 3) the BRBs remaining elastic under the design wind loads corresponding to a 137 km/h basic wind speed calculated using Method 2 in ASCE7–5 [28]. Hence, the structure is expected to develop inelastic response during a RTHS involving strong earthquake ground motions.

For the purpose of the RTHS, the original design of the building was modified by placing nonlinear viscous dampers between the ends of each outrigger truss and adjacent perimeter columns, as shown in Fig. 1 (c) and in Fig. 3. The orientation of the outrigger system in the N-S direction and lack of a load path to the BRBFs in the E-W direction results in the dampers being engaged only under N-S loading and torsion. The building has a rectangular floor plan and therefore axial deformation develops over the height of the structure from torsional warping, which causes the dampers in the outriggers to deform and dissipate energy. The axial stiffness of the perimeter columns and the axial and bending stiffness of the outrigger truss members were increased by a factor of 3 to make the dampers more effective in suppressing dynamic vibrations [13].

3. Real-time hybrid simulation configuration

3.1. Integration of the equations of motion

The analytical and experimental substructures of the RTHS consist of a 3-D finite element model of the building and one full scale nonlinear viscous damper, respectively, where the former is shown in Fig. 1. A flowchart of the integration algorithm for performing the RTHS is given in Fig. 2. The RTHS performed herein is based on the explicit model-based dissipative model-based MKR-α integration algorithm [29] to integrate the weighted equations of motion, where:

$$\boldsymbol{M}\widehat{\boldsymbol{a}}_{i+1} + \boldsymbol{C}\boldsymbol{v}_{i+1-\alpha_f} + \boldsymbol{R}^e_{i+1-\alpha_f}\left(\boldsymbol{u}^e_{i+1-\alpha_f}, \boldsymbol{v}^e_{i+1-\alpha_f}\right) + \boldsymbol{R}^a_{i+1-\alpha_f}\left(\boldsymbol{u}^a_{i+1-\alpha_f}, \boldsymbol{v}^a_{i+1-\alpha_f}\right) = \boldsymbol{F}_{i+1-\alpha_f} \tag{1}$$

$\boldsymbol{M}$ and $\boldsymbol{C}$ that appear in Eq. (1) are the analytically modeled mass and inherent damping matrices of the system, respectively. $\boldsymbol{R}^e_{i+1-\alpha_f}$, $\boldsymbol{R}^a_{i+1-\alpha_f}$, and $\boldsymbol{F}_{i+1-\alpha_f}$ are the weighted restoring force vector of the experimental substructure, the weighted restoring force vector of the analytical substructure, and the weighted forcing function, respectively, $\boldsymbol{u}^e_{i+1-\alpha_f}$ and $\boldsymbol{v}^e_{i+1-\alpha_f}$ are the weighted displacement and velocity vectors for the experimental substructure, respectively, while $\boldsymbol{u}^a_{i+1-\alpha_f}$ and $\boldsymbol{v}^a_{i+1-\alpha_f}$ are the weighted displacement and velocity vectors for the analytical substructure, respectively. The weighting of each of these quantities is determined by applying Eq. (2) to response quantities at

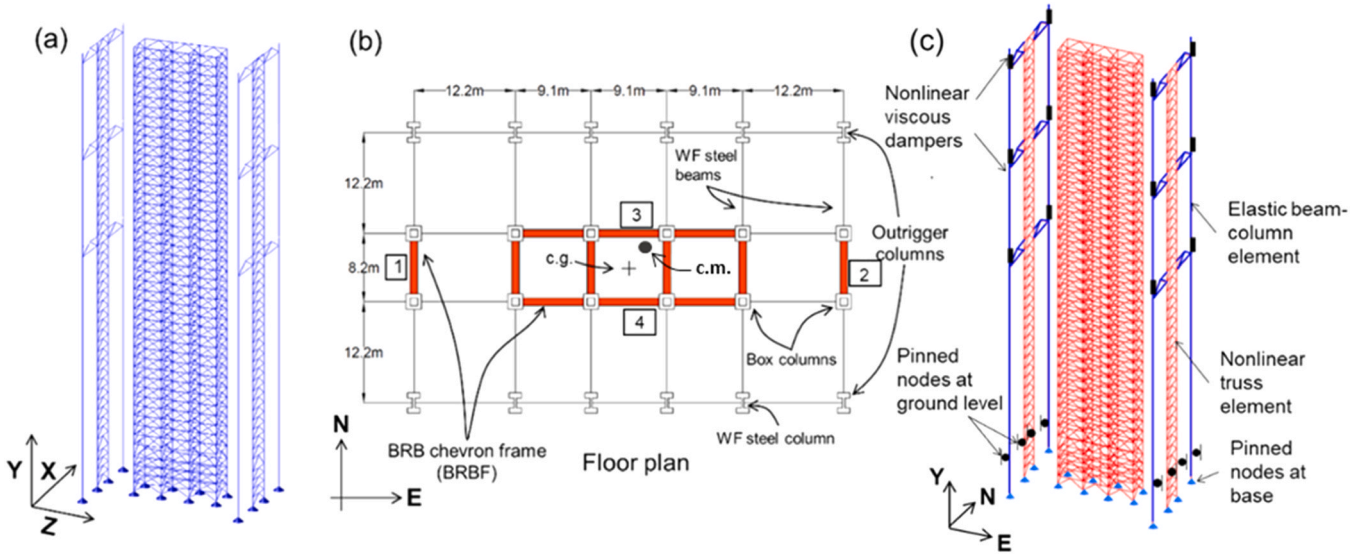

Fig. 1. Prototype 40-story tall building: a) isometric view; b) floor plan; and (c) analytical substructure for RTHS with experimental substructure-modeled dampers shown at either the NW or NE 30th story dampers (see Fig. 3 for damper configuration).

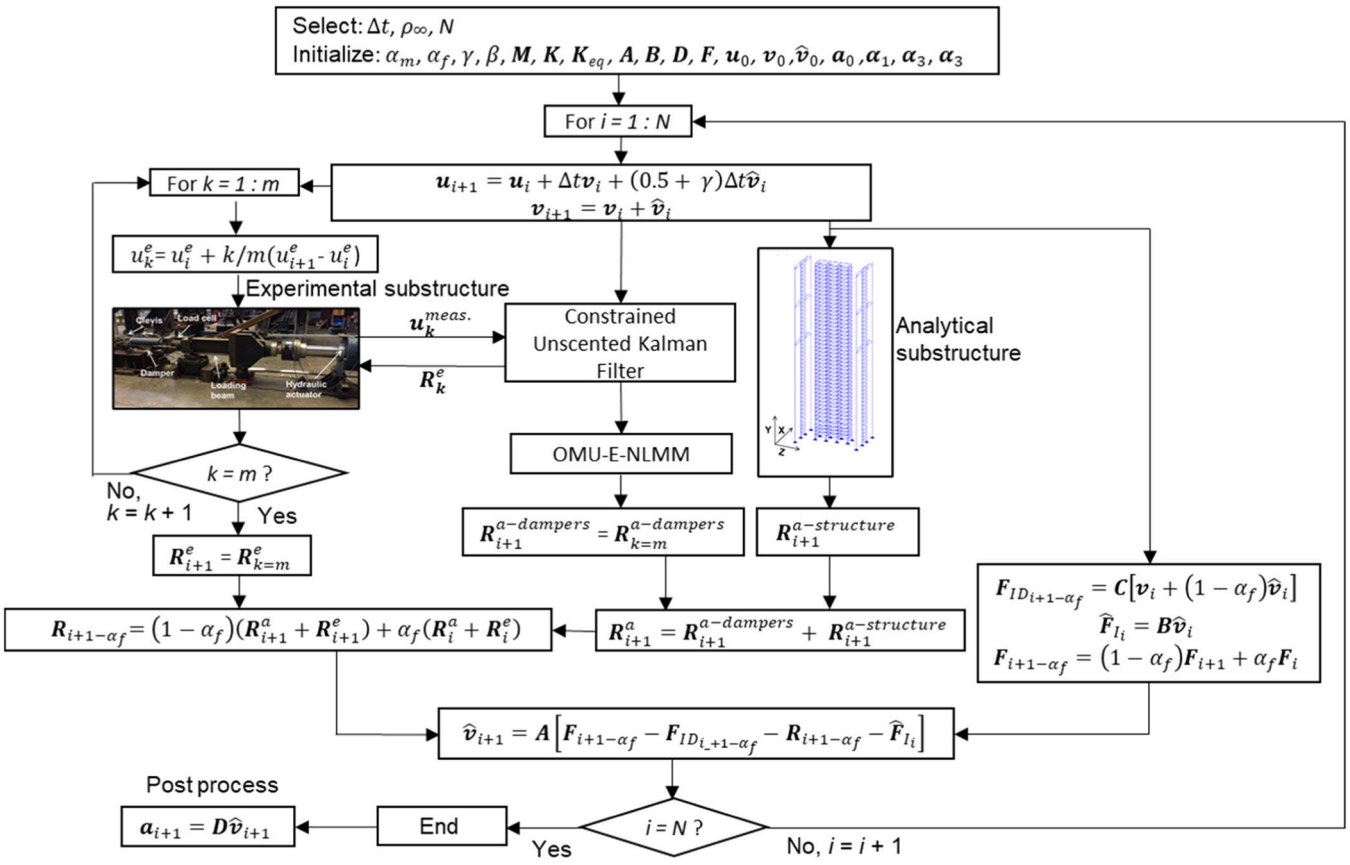

Fig. 2. RTHS configuration using the MKR-α integration algorithm.

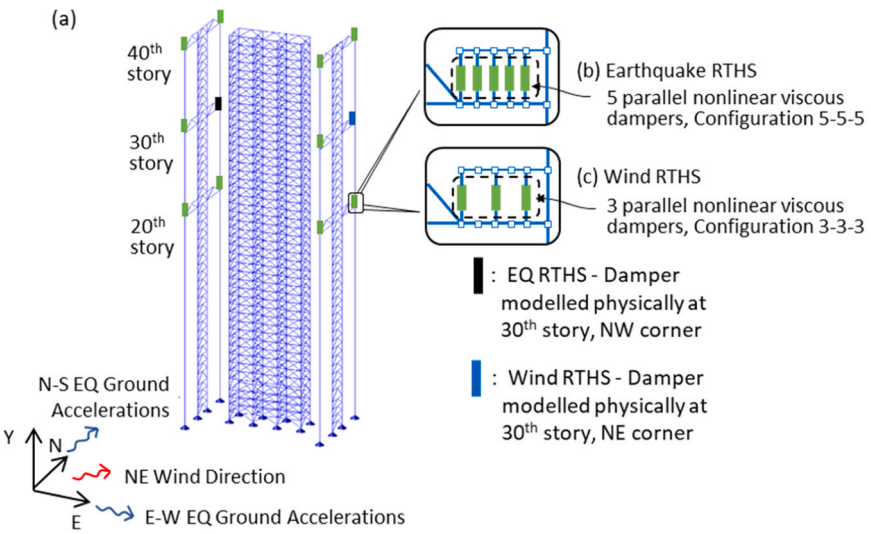

Fig. 3. Locations of viscous dampers at corners of floor plan: (a) at ends of outrigger trusses at 20th, 30th, and 40th stories, and configurations for (b) earthquake RTHS, and (c) wind RTHS; building is subjected to either bi-directional earthquake ground motions or NE wind, as shown.

time step i+1 and i:

$$(\bullet)_{i+1-\alpha_f} = (1-\alpha_f)(\bullet)_{i+1} + \alpha_f(\bullet)_i \tag{2}$$

where α_f is a weighting factor defined later. In Eq. (1) $\widehat{\boldsymbol{a}}_{i+1}$ is the weighted acceleration vector defined as:

$$\widehat{\boldsymbol{a}}_{i+1} = (\boldsymbol{I} - \boldsymbol{\alpha}_3)\boldsymbol{a}_{i+1} + \boldsymbol{\alpha}_3\boldsymbol{a}_i \tag{3}$$

In Eq. (3) $\boldsymbol{a}_{i+1}$ and $\boldsymbol{a}_i$ are the acceleration vectors at time step $i+1$ and i, respectively, and $\boldsymbol{\alpha_3}$ is a matrix of integration parameters that is defined later.

The equations of motion are integrated using the explicit-based relationships given in Eqs. (4) and (5), where $\boldsymbol{u}$, $\mathbf{v}$, and $\boldsymbol{a}$ are the vectors of displacement, velocity, and accelerations, respectively, Δt is the time step, and i and $i+1$ are associated with time step i and $i+1$, respectively.

$$\boldsymbol{v}_{i+1} = \boldsymbol{v}_i + \Delta t\boldsymbol{\alpha_1}\boldsymbol{a}_i \tag{4}$$

$$\boldsymbol{u}_{i+1} = \boldsymbol{u}_i + \Delta t \boldsymbol{v}_i + \Delta t^2 \boldsymbol{\alpha_2} \boldsymbol{a}_i \tag{5}$$

In the above Eqs. (3), (4) and (5), $\boldsymbol{\alpha_1}$, $\boldsymbol{\alpha_2}$, and $\boldsymbol{\alpha_3}$ are matrices of integration parameters of size n x n, where n is the number of DOF of the system. The integration parameters are formulated [29,30] such that the MKR-α integration algorithm possesses numerical energy dissipation and has the same dispersion characteristics as the Generalized-α method [31], where

$$\boldsymbol{\alpha_1} = \boldsymbol{\alpha}^{-1}\boldsymbol{M}, \boldsymbol{\alpha_2} = (0.5+\gamma)\boldsymbol{\alpha_1}, \quad \boldsymbol{\alpha_3} = \boldsymbol{\alpha}^{-1}\left[\alpha_m \boldsymbol{M} + \alpha_f \gamma \Delta t \widetilde{\boldsymbol{C}} + \alpha_f \beta \Delta t^2 \widetilde{\boldsymbol{K}}\right] \tag{6a,b,c}$$

In Equation (6c) $\widetilde{\boldsymbol{C}}$ and $\widetilde{\boldsymbol{K}}$ are the damping and elastic stiffness matrices of the complete system, respectively, which are based on the system's inherent damping matrix $\boldsymbol{C}$ and the stiffness matrix $\boldsymbol{K}$ for the analytical substructure in addition to the contribution of the experimental substructure damping and stiffness matrices $\boldsymbol{C}_{eq}$ and $\boldsymbol{K}_{eq}$, respectively, whereby

$$\widetilde{\boldsymbol{C}} = \boldsymbol{C} + \boldsymbol{C}_{eq}, \quad \widetilde{\boldsymbol{K}} = \boldsymbol{K} + \boldsymbol{K}_{eq} \tag{7}$$

For the RTHS performed herein, which involve nonlinear viscous dampers, the equivalent linear stiffness and damping of the dampers was established using the linearized Kelvin-Voigt model at the fundamental frequency of the structure [32].

To expedite the integration of the weighted equations of motion for performing the RTHS a super element that is described in Section 5 is used to reduce the number DOF of the model, and therefore the size of the matrices $\boldsymbol{M}$, $\widetilde{\boldsymbol{C}}$ and $\widetilde{\boldsymbol{K}}$, which in turn reduces the size of the integration parameters matrices $\boldsymbol{\alpha_1}$, $\boldsymbol{\alpha_2}$, and $\boldsymbol{\alpha_3}$. Consequently, there is a reduction in the matrix calculation effort during the RTHS since the size of the matrices are smaller. To further reduce the computational demand, Eq. (1) through (6) are combined, as shown in Fig. 2, to establish the following recursive relationship:

$$\widehat{\boldsymbol{v}}_{i+1} = \boldsymbol{A}\left[\boldsymbol{F}_{i+1-\alpha_f} - \boldsymbol{F}_{ID_{i+1-\alpha_f}} - \boldsymbol{R}_{i+1-\alpha_f} - \widehat{\boldsymbol{F}}_{I_i}\right] \tag{8}$$

where

$$\boldsymbol{a}_{i+1} = \boldsymbol{D}\widehat{\boldsymbol{v}}_{i+1}, \quad \boldsymbol{D} = \frac{1}{\Delta t}\ \boldsymbol{\alpha}_1^{-1}, \quad \boldsymbol{A} = \Delta t \boldsymbol{\alpha_1}[\boldsymbol{M} - \boldsymbol{M}\boldsymbol{\alpha_3}]^{-1} \tag{9a,b,c}$$

and

$$\begin{aligned}\boldsymbol{F}_{ID_{i+1-\alpha_f}} &= \boldsymbol{C}\left[\boldsymbol{v}_i + (1-\alpha_f)\widehat{\boldsymbol{v}}_i\right], \quad \boldsymbol{R}_{i+1-\alpha_f} \\ &= (1-\alpha_f)\left(\boldsymbol{R}^a_{i+1} + \boldsymbol{R}^e_{i+1}\right) + \alpha_f\left(\boldsymbol{R}^a_i + \boldsymbol{R}^e_i\right), \quad \widehat{\boldsymbol{F}}_{I_i} = \boldsymbol{B}\widehat{\boldsymbol{v}}_i\ , \boldsymbol{B} \\ &= \frac{1}{\Delta t}\boldsymbol{M}\boldsymbol{\alpha_3} \quad \boldsymbol{\alpha}_1^{-1},\end{aligned} \tag{10a,b,c,d}$$

Equations (6b) and (9a,b) are used to rewrite Eqs. (4) and (5) to include $\widehat{\boldsymbol{v}}_i$, where

$$\boldsymbol{v}_{i+1} = \boldsymbol{v}_i + \widehat{\boldsymbol{v}}_i \tag{11}$$

$$\boldsymbol{u}_{i+1} = \boldsymbol{u}_i + \Delta t \boldsymbol{v}_i + (0.5+\gamma)\Delta t \widehat{\boldsymbol{v}}_i \tag{12}$$

As will be discussed later, the use of Eqs. (8), (11), and (12) avoid the need for calculating the acceleration vector $\boldsymbol{a}_{i+1}$, thereby further expediating the calculation process during each time step of the RTHS.

The quantities γ, β, α_f, and α_m that appear in the above equations are scalars that are related to each other by:

$$\gamma = 0.5 - \alpha_m + \alpha_f\ , \qquad \beta = 0.5(0.5+\gamma) \tag{13ab}$$

The parameters α_f and α_m are related to the high-frequency spectral radius ρ_∞ as follows:

$$\alpha_f = \frac{\rho_\infty}{\rho_\infty + 1}\ , \qquad \alpha_m = \frac{2\rho_\infty{}^3 + \rho_\infty{}^2 - 1}{\rho_\infty{}^3 + \rho_\infty{}^2 + \rho_\infty + 1} \tag{14a,b}$$

Hence, the MKR-α integration algorithm has only one free parameter ρ_∞, which varies in the range of $0 \le \rho_\infty \le 1$. The parameter ρ_∞ controls the amount of numerical energy dissipation, where $\rho_\infty = 1$ and 0 impose zero and the maximum numerical energy dissipation, respectively.

Integrating the equations of motion involves first initializing various quantities, as identified in Fig. 2, where the vector of initial acceleration $\boldsymbol{a}_0$ is obtained based on satisfying equilibrium for the selected conditions for initial displacement $\boldsymbol{u}_0$ and initial velocity $\boldsymbol{v}_0$:

$$\boldsymbol{M}\boldsymbol{a}_0 = \boldsymbol{F}_0 - \widetilde{\boldsymbol{C}}\boldsymbol{v}_0 - \widetilde{\boldsymbol{K}}\boldsymbol{d}_0 \tag{15}$$

The process then continues where for each time step: (1) the vector of target velocities $\boldsymbol{v}_{i+1}$ and displacements $\boldsymbol{u}_{i+1}$ are determined from Eqs. (11) and (12); (2) the target displacements are then imposed onto the experimental and analytical substructures to obtain their respective vectors of restoring forces $\boldsymbol{R}^e_{i+1}$ and $\boldsymbol{R}^a_{i+1}$, respectively; and, (3) $\widehat{\boldsymbol{v}}_{i+1}$ is determined using Eq. (8). $\boldsymbol{R}^e_{i+1}$ is obtained by measuring the restoring forces developed in the experimental substructure, while $\boldsymbol{R}^a_{i+1}$ is obtained from a state determination that is performed on each element of the analytical model, $\boldsymbol{R}^{a-structure}_{i+1}$, which is then summed with the contribution of the analytically modeled dampers' restoring forces $\boldsymbol{R}^{a-dampers}_{i+1}$, where

$$\boldsymbol{R}^a_{i+1} = \boldsymbol{R}^{a-dampers}_{i+1} + \boldsymbol{R}^{a-structure}_{i+1} \tag{16}$$

$\boldsymbol{R}^{a-dampers}_{i+1}$ is determined from applying the online model updating algorithm's model parameters in the Constrained Unscented Kalman Filter block to the damper models (identified as OMU-E-NLMN in Fig. 2, and discussed later). The structure's acceleration vector $\boldsymbol{a}_{i+1}$ is not required to be computed during the RTHS, as implied in Fig. 2, thereby expediting the calculations during the RTHS. This is critical when performing a RTHS, where the computational resources are preserved to perform only the required computations during the RTHS to enable the simulation to be conducted in real-time. The system's acceleration vector $\boldsymbol{a}$ for each time step (e.g., $\boldsymbol{a}_{i+1}$) can be recovered following the RTHS by using Equation (9a), where $\widehat{\boldsymbol{v}}_{i+1}$ has been saved for each time step during the RTHS.

The integration of the weighted equations of motion during the RTHS used a time step size of $\Delta t = 11/1024$ s for the MKR-α algorithm, with ρ_∞ equal to 0.5 for the earthquake and 0.75 for the wind simulations. The values for Δt and ρ_∞ were determined from numerical convergence studies to be suitable values for conducting accurate RTHS.

3.2. Test matrix

The test matrix for the RTHS is given in Table 1 and includes multi-axis earthquake and wind loading natural hazards. The earthquake loading was based on the orthogonal components of the 1989 Loma Prieta ground motion scaled to the MCE hazard level, which has a 2475-year return period [26]. The wind load is imposed in the NE direction on the building and has a 177 km/h basic wind speed with a 700-year mean return interval. The wind load history was obtained by placing a 1/150 scale aerodynamic model of the tall building in a wind tunnel to measure wind pressures and then scaling them to full scale. The directions of the applied earthquake and wind loading are illustrated in Fig. 3. Further details about the earthquake record and wind loading are presented in Section 4 Description of Natural Hazards.

The configuration of the dampers in the building is given in Table 1 and includes Configurations 5–5-5 and 3–3-3. Configurations 5–5-5 and 3–3-3 indicate five and three dampers, respectively, acting in parallel between the ends of each outrigger truss and adjacent perimeter column at the 20th, 30th, and 40th stories, as illustrated in Fig. 3. Hence, there are a total of 60 dampers in the building for Configuration 5–5-5 for the

Table 1
RTHS test matrix.

Test ID	Natural hazard	Damper configuration	Total number of dampers	ATS coefficients configuration					
				Coefficient	Floor value	Ceiling value	Maximum rate of change	Initial value	RMS Threshold
1	Earthquake	5-5-5	60	*a0*	0.8	1.2	2×10^{-3}	0.984	1 mm
				a1	0	3×10^{-2}	5×10^{-5}	0.017	
				a2	0	2×10^{-4}	1×10^{-6}	1×10^{-4}	
2	Wind	3-3-3	36	*a0*	1	1	2×10^{-3}	1	1 mm
				a1	0	4×10^{-2}	5×10^{-5}	0.015	
				a2	0	0	1×10^{-6}	0	

earthquake RTHS, and 36 dampers for Configuration 3–3-3 for the wind RTHS. The earthquake loading resulted in large deformation demand on the dampers which caused the damper stroke limit to be exceeded when using Configuration 3–3-3. Consequently, the number of dampers in the earthquake RTHS was increased to five to reduce the damper deformations during the earthquake. The purpose of this paper is to present a framework for performing 3-D RTHS of a tall building. The response of the building under earthquake and wind loading are discussed separately and is not intended to be compared, and therefore the number of dampers in the model being different for these two loading conditions was deemed to be acceptable.

Table 1 includes information related to the ATS compensator for the actuator used in the experimental substructure. Details about the compensator are presented later in Section 7.

4. Description of natural hazards

4.1. Earthquake

The components RSN802_LOMAP_STG000 and RSN802_LOMAP_STG090 of the 1989 Loma Prieta earthquake ground motions from the PEER data base [33] that were recorded at the Saratoga Aloha Avenue station were used for the earthquake RTHS. The uniform hazard spectra based on the building's location was calculated and used as the target spectrum for scaling the ground motions [26]. All ground motion pairs were scaled by minimizing the error between the geometric mean of the scaled ground motion and the uniform hazard spectra between the period range 0.5 to 10 s, with error weights of 10 % for the period range of 0.5–3 s, 60 % for the period range of 3–7 s, and 30 % for the of period range 7–10 s in accordance with Moehle et al. [26]. The record had a low-pass filter with a cutoff frequency of 0.1 Hz applied, ensuring that the long-period excitation content was included as required for tall building performance assessment [26]. The acceleration time histories are shown in Fig. 4(a) and (b), where the scale factor is 1.98 for the MCE hazard level. The scaled components RSN802_LOMAP_STG000 and RSN802_LOMAP_STG090 of the record were imposed in the N-S and E-W directions of the building, respectively. The response spectra of the scaled ground motions along with the MCE target hazard spectrum are shown in Fig. 4(c). The fundamental period of the building in the E-W and N-S direction are $T_1^{EW} = 4.07$ s and $T_1^{NS} = 6.71$ s, respectively, where it is evident in Fig. 4(c) that the spectral accelerations in the E-W direction at a period of T_1^{EW} are almost three times that in the N-S direction at T_1^{NS}.

4.2. Wind

The 1/150 length scale factor aerodynamic model of the building was tested in the Wall of Wind FIU wind tunnel to measure wind pressure coefficient time histories. This involved using 336 pressure taps distributed around the four sides of the model, see Fig. 5(a) and (b). The wind tunnel's rotating table (see Fig. 5(a)) was oriented at 45 degrees, whereby a NE direction of wind with respect to the building's floor plan (see Fig. 3) was generated in the wind tunnel when measuring the non-dimensional pressure coefficients $C_p(t)$.

The wind pressure $P_r(t)$ acting on the full-scale building was obtained using $P_r(t) = 0.5\rho_{air}V_{SF}^2C_p(t)$, where ρ_{air} is the air density of 1.161 Kg/m^3, and V_{SF} the target mean wind speed at the roof level. V_{SF} is determined using the two-step procedure given in Kolay [34] and in

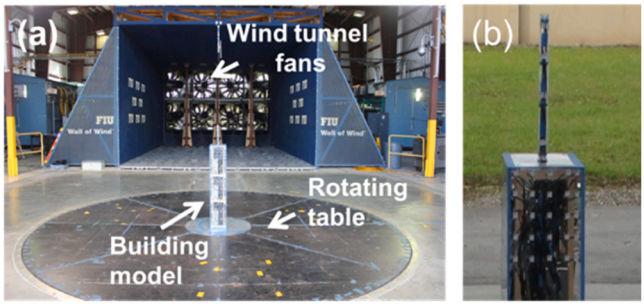

Fig. 5. (a), (b) 1/150 scale aerodynamic model of building placed in wind tunnel (courtesy of Florida International University).

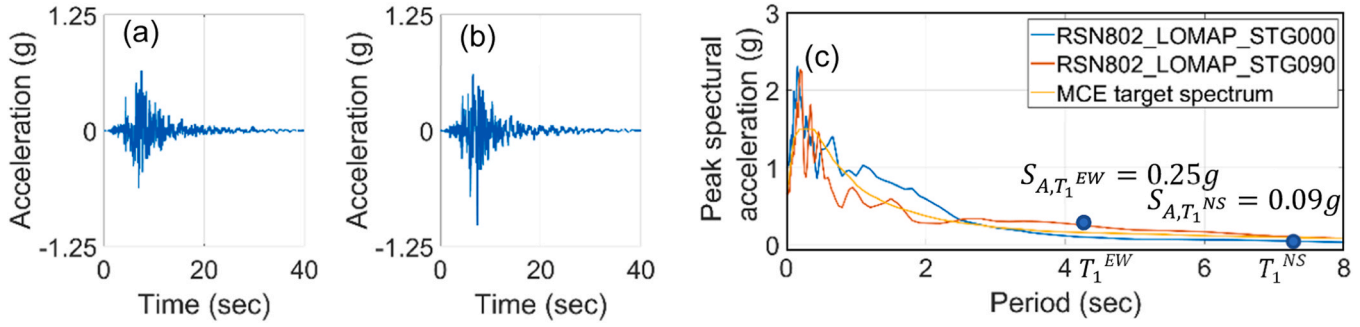

Fig. 4. Ground acceleration scaled to the maximum considered earthquake: a) building's E-W direction; and, b) building's N-S direction. c) response acceleration spectrum of each individual ground motion component and target spectrum scaled to the Maximum Considered Earthquake hazard level. (components STG000 and STG090 are used in the N-S and E-W directions of the building, respectively).

Simiu and Scanlan [35] in conjunction with a selected basic wind speed. The non-dimensional pressure time history at each floor level is obtained by linear interpolation of the pressure time history between pressure taps in the vertical direction. The pressure is then multiplied by its tributary area to obtain floor wind loads that include two orthogonal horizontal and torsional loads. The non-dimensional pressure coefficients $C_p(t)$ were measured at a sampling frequency of 520 Hz. The full -scale prototype time interval for the force time history was determined by $\Delta t_{fs} = D_{fs}U_{ss}\Delta_{ts}/D_{ss}U_{fs}$, where Δ_{ts} is the sampling period of the wind tunnel test, D_{fs}/D_{ss} is the geometric scale of building model for the wind tunnel test (equal to 150), and U_{ss}/U_{fs} is the ratio between the reference wind speed of the small (V_{SF}) to the full scale model at the eave height of the prototype structure for exposure B. The mean wind speed at the roof of the building (i.e., U_{ss}) during the wind tunnel testing was 64 km/h. The duration of the wind storm for the RTHS was 325 s, where during the first and last 30 s of the test the wind load was ramped up and down, respectively. The history of wind pressures were integrated to obtain the history of lateral wind loads in the E-W and N-S directions and torsional wind loads for each of the 40 floors of the structure. The time history of the floor wind loads at the 20th, 30th, and the 40th floors are shown in Fig. 6(a), (b), and (c), respectively.

5. Analytical substructure

The 3-D analytical substructure for the RTHS is shown in Fig. 1(c) where the model was created using the computer program HyCom-3D developed by Ricles et al. [36]. The X-Y-Z global coordinate system for the model is shown in Fig. 1, where the N-S direction coincides with the X- axis, the E-W direction with the Z- axis, and the Y-axis with the vertical elevation of the building. The beams and columns of the building were modeled using linear elastic beam-column elements based on their member section properties. The moments about their strong axis at the beam ends adjacent to the columns were released (i.e., the beams are pin-connected to the columns). The BRBs were modeled using explicit formulated nonlinear truss elements with the Giuffré -Menegotto-Pinto material model [37,38]. The core of each BRB was designed to constrain yielding of the brace to occur was 70 % member's length. The remaining 30 % of the BRB's length is modeled as rigid to account for the large stiffness of the gusset plates, BRB connections, and column depth. The outrigger truss chord members and columns were modeled using elastic beam-column elements. The floor mass is lumped at a lean-on-column located at the center of the floor plan, which includes the translation and rotational inertia in the plane of the floor diaphragm due to the distributed floor mass. The lean-on column is used to account for the P-Δ effect in the building and gravity loads are applied to it. The floor mass has a 5 % eccentricity in both horizontal directions to account for accidental torsion during the earthquake RTHS, while no mass eccentricity was considered in the case of the wind RTHS. The reason for incorporating an eccentricity in the former case was to include torsion in the earthquake RTHS. The wind loading did not require an accidental eccentricity due to the nonuniformity of the wind pressures around the circumference that created torsional wind loading. The mass is shifted towards the NE direction of the floor plan at each floor level for the earthquake RTHS in order to induce torsional seismic effects (see Fig. 1(b), where the center of mass is identified as *c.m.* and distanced from the center of rigidity that is identified as *c.g.*).

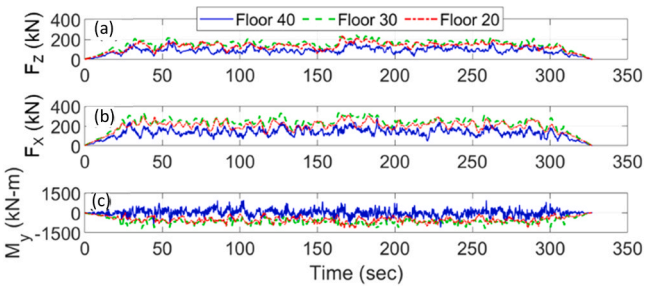

Fig. 6. Measured wind tunnel full-scale time history of wind loading at 20th, 30th floors and roof level; (a) lateral wind loads in the E-W direction; (b) lateral wind loads in the N-S direction; and, (c) torsional wind loads.

The nodes at the base of the building are restrained in all three translational directions using a pin-ended boundary condition between the base of the columns and a rigid foundation. A rigid floor diaphragm was created by placing a master node at the center of mass at each floor level to which the translational and rotational degrees-of-freedom of the remaining nodes of the floor are slaved. The earthquake effective forces and wind loads are applied at the master node of each floor, including any story torsional loads due to wind. The inherent damping of the building is modeled using 2 % modal damping for modes 1 through 30 with stiffness proportional damping for modes 31 and beyond. Using modal damping for nonlinear seismic time history response is consistent with the recommendation by Chopra and McKenna [39] and Qian et al., [40].

The analytical substructure model included 1317 nodes and 3974 degrees of freedom. Because of the large number of degrees of freedom and the associated computational cost, all elastic elements in the model, except for the outrigger trusses and outrigger columns, were modeled using a super element to condense the large number of degrees of freedom without compromising the ability of the analytical model to capture the nonlinear behavior of the building that occurred in the BRBs. The elastic elements which modeled the columns and beams of the BRBFs were included in the super element. The super element in effect applied static condensation to the model's stiffness matrix to reduce the number of degrees of freedom. Reducing the number of degrees of freedom reduces the size of the matrices used in the RTHS calculations, expediting these calculations to be completed within the time step Δt and thereby the simulation to be run in real time. The use of the super element is appropriate because of the following reasons: 1) the beams and columns are designed to remain elastic when the BRBs yield [26]; 2) the floor mass is lumped at each floor level, and therefore there is no need to implement dynamic sub-structuring methods such as the Craig-Bampton reduction method [41]; and, 3) the translational and torsional loads are applied at the master node of each floor diaphragm, whose degrees of freedom are retained. Using the super element reduced the number of degrees of freedom from 3974 to 1429. The resulting analytical substructure model had 1080 nonlinear truss elements to model the BRBs, 44 lean-on column elements to model the lean-on columns, and one super element to model the remaining members of the building. The gravity beams between the inner core of the building and perimeter columns, as well as the perimeter gravity columns, were excluded in the model.

The super element in HyCom-3D requires the stiffness matrix $\boldsymbol{K}_{super}$ to be defined. To obtain the stiffness matrix for the super element, the flexibility for the super element is first formed. This is achieved by systematically applying individual unit forces to each degree of freedom of the super element model, with all of the degrees of freedom from which the retained degrees of freedom NRDOF are sought. Only the nodal displacements and rotations corresponding to the retained degrees of freedom for NRDOF load cases are retained to arrive at the condensed flexibility matrix for the super element. This matrix is then inverted to obtain $\boldsymbol{K}_{super}$.

The number of degrees of freedom in the analytical substructure RTHS model, NRDOF, as noted above, is equal to 1429. The final stiffness matrix for the analytical substructure, $\boldsymbol{K}$, of size NRDOF by NRDOF is obtained by appropriately adding the terms of the stiffness matrices of the nonlinear truss elements that model the BRBs and the lean-on column elements to the super element's stiffness matrix $\boldsymbol{K}_{super}$. The retained degrees of freedom about the X and Z axes of the global coordinate system and rotation about the Y global axis of the slaved nodes at each

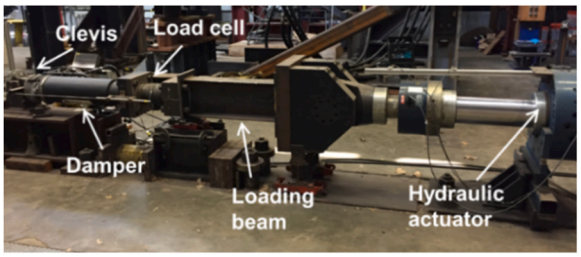

Fig. 7. Real-time hybrid simulation experimental substructure.

floor are constrained to a master node at that floor when generating $\boldsymbol{K}_{super}$. The BRB and lean-on column elements, which are connected to slaved nodes, therefore have their degrees of freedom slaved to the appropriate master node.

6. Experimental substructure

The experimental substructure consisted of a full scale nonlinear viscous damper with a 600 kN load capacity and a ±125 mm stroke, and is shown in Fig. 7. The damper is connected to a 1700 kN capacity hydraulic actuator through a loading beam resting on a steel roller. The actuator is ported with three high-flow 2080 lpm servo-valves that enables a maximum velocity of 1.140 m/sec. to be achieved. A load cell is placed between the damper and the loading beam in which the measured load cell reading is related to the restoring force $\boldsymbol{R}^e_{i+1}$ of the experimental substructure used to integrate the equations of motion. The measured load cell reading is a scalar that is multiplied by the number of dampers at the end of each outrigger truss (i.e., five for the earthquake and three for the wind RTHS) to simulate the number of dampers that act in parallel in accordance with the damper layout configuration shown in Fig. 3(b) and (c), where the result is the experimental substructure restoring force $\boldsymbol{R}^e_{i+1}$.

The experimental substructure's damper is located at the 30th floor in the NW corner for the earthquake RTHS and at the NE corner for the wind RTHS, as indicated in Fig. 3. It is placed at the location in the structure where the largest demand is expected to occur during the earthquake and wind, established from trial numerical simulations. As discussed below, this is necessary in order to achieve accurate results via the online model updating, whereby the updating is based on damper deformations in the numerically modeled dampers that are less than that of the experimental substructure's damper.

7. Servo-hydraulic actuator adaptive compensator

As mentioned previously, the second order ATS compensator [25] was used to compensate for servo-hydraulic actuator delay and amplitude error in the experimental substructure's actuator during the RTHS. The ATS compensator consists of three adaptable coefficients a_0, a_1, and a_2 that are used to arrive at the actuator compensated command displacement u^c_k, where at time step k:

$$u^c_k = a_{0,k}x^t_k + a_{1,k}\dot{x}^t_k + a_{2,k}\ddot{x}^t_k \tag{17}$$

The coefficients in Eq. (17) adapt for each time step k during a RTHS in accordance with the control law described in Chae et al. [25], where u^c_k is the prescribed compensated displacement for the servo-hydraulic actuator that minimizes actuator delay and amplitude error between the actuator targeted and compensated command motions. In Eq. (17) x^t_k, $\dot{x}^t_k$, and $\ddot{x}^t_k$ are the target displacement, velocity, and acceleration of the actuator based on the integration of the equations of motion and transformed to the actuator extensional degree of freedom for time step k. The measured actuator displacements, velocities and accelerations are sampled over a one-second moving window (where a time step size of Δt = 11/1024 s was used) and a regression analysis performed to arrive at the values of the coefficients for time step i that minimizes the error between the target and measured motions actuator over the moving window [25]:

$$\boldsymbol{A} = \left(\boldsymbol{X_m}^T\boldsymbol{X_m}\right)^{-1}\boldsymbol{X_m}^T\boldsymbol{U_c} \tag{18}$$

where $\boldsymbol{A} = [a_{0k},\ a_{1k},\ a_{2k}]^T$, $\boldsymbol{X_m} = \left[\boldsymbol{x^m}, \dot{\boldsymbol{x}}^{\boldsymbol{m}}, \ddot{\boldsymbol{x}}^{\boldsymbol{m}}\right]$, $\boldsymbol{x^m} = \left[x^m_{k-1}\ \ x^m_{k-2}\ \ \cdots\ \ x^m_{k-q}\right]^T$, and $\boldsymbol{U_c} = \left[u^c_{k-1}\ \ u^c_{k-2}\ \ \cdots\ \ u^c_{k-q}\right]^T$. $\boldsymbol{x^m}$, $\dot{\boldsymbol{x}}^{\boldsymbol{m}}$, $\ddot{\boldsymbol{x}}^{\boldsymbol{m}}$are the vector of the measured actuator displacement, velocity, and accelerations over the moving window of a 1 s width (associated with the value of q) and $\boldsymbol{U_c}$.is the vector of computed compensated actuator displacements obtained from Eq. (17) over this moving window. Additional details of the ATS compensator can be found in Chae et al. [25]. Table 1 lists the configuration of the coefficients ATS for the earthquake and wind RTHS, which includes the floor and ceiling limit values, maximum allowable rate of change, initial values, and RMS threshold that when exceeded triggers the algorithm to adapt the values of the coefficients within the floor and ceiling limit values.

8. Nonlinear viscous damper online model updating

As noted above, the building in the study reported herein has multiple nonlinear viscous dampers placed vertically between the end of each outrigger truss and outrigger perimeter column throughout the building. These nonlinear viscous dampers, excluding the one modeled physically, because of the limited number of available physical dampers are modeled analytically using the explicit non-iterative online updating model for the nonlinear Maxwell model that appears within the OMU-E-NLMM block in Fig. 2. A schematic of the nonlinear Maxwell model is shown in Fig. 8, where the model parameters include an elastic spring of stiffness K_d, a dashpot with a coefficient value of C_d, and velocity exponent α. The explicit non-iterative online updating model for the nonlinear Maxwell model is based on the Explicit Nonlinear Maxwell Model (E-NLMM) developed by the authors [42] and is given by:

$$f_{d_{k+1}} = f_{d_k} - K_d\Delta t\left|\frac{f_{d_k}}{C_d}\right|^{\frac{1}{\alpha}} sign\left(f_{d_k}\right) + K_d\left(u_{d_{k+1}} - u_{dk}\right) \tag{19}$$

In Eq. (19) f_d and u_d are the damper force and deformation, respectively, with the subscript k and k+1 associated with time step k and k+1, respectively, and Δt is the time step size.

The unscented Kalman filter [43] in its constrained form [44–46] is used to identify the damper model parameters in real-time during the RTHS. The constrained unscented Kalman filter (CUKF) has low computational effort, which is beneficial in a RTHS, since it does not require the determination of the Jacobian [47]. The model parameters for the E-NLMM are state variables, requiring a total of 7 sigma points for the CUKF. The CUKF is used to ensure that the sigma points of the UKF remain within a desired range to avoid divergence of the parameters, which would result in poor estimates for the damper force f_d which are excessively large and which can cause the RTHS to become unstable. It was found that the floor and ceiling values for the CUKF that prevented instabilities in the RTHS were 0.2 and 2.0 times the initial mean value of each parameter K_{d0}, C_{d0}, and α_0. The initial mean values for the parameters were determined by performing characterization testing on the damper using the experimental setup described in Section 6, where the damper was subjected to a 75 mm amplitude sinusoidal

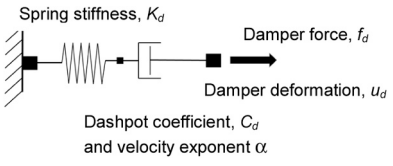

Fig. 8. Nonlinear Maxwell model.

Table 2
Identified parameters of the nonlinear Maxwell model (E-NLMM).

Displacement amplitude (mm)	Frequency range (Hz)	Spring stiffness K_{d0} (kN/m)	Dashpot coefficient C_{d0} (kN-(sec/m)$^{\alpha}$)	Velocity exponent α_0
75	0.25-1.00 Hz	1.02E5	708	0.457

displacement with a frequency range of 0.25 to 1.0 Hz. Values for K_{d0}, C_{d0}, and α_0 were identified using Particle Swarm Optimization [48], and are given below in Table 2. The spring stiffness K_{d0} is seen to be six orders of magnitude larger than the velocity exponent α_0, which can lead to an ill-conditioned covariance matrix for the state variables during the model updating. This is discussed further below.

In the CUKF the initial values of the mean state variables $\hat{\mathbf{x}}_{k=0|k=0} = \begin{bmatrix} K_{d_0} & C_{d0} & \alpha_0 \end{bmatrix}^T$ need to be specified, along with the 3×3 process noise covariance matrix $\mathbf{Q}$, the measurement noise covariance R, and the 3×3 covariance matrix $\mathbf{P}_{k=0|k=0}$ for the state variables. Weights $W_j^{(m)}$ and $W_j^{(c)}$ for each sigma point associated with the mean and covariance are predefined [49], where:

$$W_{j=0}^{(m)} = 1 \Big/ (L+\lambda) \tag{20}$$

$$W_{j=0}^{(c)} = \lambda \Big/ (L+\lambda) + (1-\alpha^2+\beta) \tag{21}$$

$$W_j^{(m)} = W_j^{(c)} = \frac{1}{(2L+2\lambda)}, \quad j = 1, \ldots, 2L \tag{22}$$

In Eq. (22) $L = 3$, which is the dimension of the state variables vector; $\lambda = \mu^2(L+\kappa) - L$ and is a scaling parameter, where μ determines the spread of the sigma points about their mean and is set to a small positive value, and κ is a secondary scaling parameter. β in Eq. (21) is used to incorporate prior knowledge of the distribution of the sigma points. μ, κ, and β are assigned the values of 1E-3, 0, and 2 respectively, in accordance with Wan and van der Merwe [49].

For each time step k of the RTHS, where $k = 1 \ldots N$, the CUKF performs the following steps:

Step 1: Define the matrix of sigma points $\boldsymbol{x}_{k-1|k-1}$ having 3 rows and $(2n+1)$ columns, where $n = 3$,

$$\boldsymbol{x}_{k-1|k-1} = \left[\hat{\boldsymbol{x}}_{k-1|k-1} \quad \hat{\boldsymbol{x}}_{k-1|k-1} + \left(\hat{\gamma} \sqrt{(L+\lambda)\boldsymbol{P}_{k-1|k-1}} \right)_{i=1,2,3} \quad \hat{\boldsymbol{x}}_{k-1|k-1} - \left(\hat{\gamma} \sqrt{(L+\lambda)\boldsymbol{P}_{k-1|k-1}} \right)_{i=1,2,3} \right] \tag{23}$$

where i denotes the column index of the positive definite covariance matrix $\boldsymbol{P}_{k-1|k-1}$. The covariance matrix in the CUKF is scaled by $\hat{\gamma} \in (0, 1)$ to enforce the constraint that the sigma points remain within their specified bounds. The value of $\hat{\gamma}$ is initialized at 1.0 and the sigma points $\boldsymbol{x}_{k-1|k-1}$ are computed from Eq. (23). If any of the sigma points fall outside their bounds (i.e., are either less than the floor value or greater than the ceiling value) then the value of $\hat{\gamma}$ is decreased incrementally with a value of 0.1 until all of the sigma points are within their bounds. Note that the calculation of $\sqrt{(L+\lambda)\boldsymbol{P}_{k-1|k-1}}$ requires that $\boldsymbol{P}_{k-1|k-1}$ be a semi-positive definite matrix, which is discussed more later.

Step 2: Predict the state vector $\hat{\boldsymbol{x}}_{k|k-1}$ and update the covariance matrix $\boldsymbol{P}_{k|k-1}^{xx}$ for the state variables

$$\boldsymbol{x}_{k|k-1} = \boldsymbol{x}_{k-1|k-1} \tag{24}$$

$$\hat{\boldsymbol{x}}_{k|k-1} = \sum_{j=0}^{2L} W_j^{(m)} * \left(\boldsymbol{x}_{k|k-1}\right)_j \tag{25}$$

$$\boldsymbol{P}_{k|k-1}^{xx} = \sum_{j=0}^{2L} W_j^{(c)} * \left(\left(\left(\boldsymbol{x}_{k|k-1}\right)_j - \hat{\boldsymbol{x}}_{k|k-1} \right) \left(\left(\boldsymbol{x}_{k|k-1}\right)_j - \hat{\boldsymbol{x}}_{k|k-1} \right)^T \right) + \boldsymbol{Q} \tag{26}$$

where $j = \{0, \ldots, 6\}$, and is the column index of the sigma points matrix.

Step3 : Predict the force $\hat{y}_k$ and update the covariance $P_{k|k-1}^{yy}$ for the predicted force of the nonlinear viscous damper residing in the experimental substructure,

$$\left(y_{k|k-1}\right)_j = h\left\{ \left(\boldsymbol{x}_{k|k-1}\right)_j, \hat{y}_{k-1}, u_{d_k}, u_{d_{k-1}}, \Delta t \right\} \tag{27}$$

$$\hat{y}_k = \sum_{j=0}^{2L} W_j^{(m)} * \left(y_{k|k-1}\right)_j \tag{28}$$

$$P_{k|k-1}^{yy} = \sum_{j=0}^{2L} W_j^{(c)} * \left(\left(y_{k|k-1}\right)_j - \hat{y}_k \right)^2 + R \tag{29}$$

where $\left(\boldsymbol{x}_{k|k-1}\right)_j = \left[K_{d_{k|k-1}} \quad C_{d_{k|k-1}} \quad \alpha_{k|k-1} \right]_j^T$, $h\{\bullet\}$ is the nonlinear measurement function (Eq. (19)), $\hat{y}_{k-1}$ is the predicted damper force from the previous time step, and u_{d_k} and $u_{d_{k-1}}$ are the experimental substructure's measured nonlinear viscous damper deformations for time step k and k-1, respectively. Both $u_{d_{k=0}}$ and $\hat{y}_{k=0}$ are initialized to zero.

Step 4: Calculate the Kalman gain vector $\mathbf{K}_k$

$$\boldsymbol{K}_k = \boldsymbol{P}_{k|k-1}^{xy} * \left(P_{k|k-1}^{yy} \right)^{-1} \tag{30}$$

where

$$\boldsymbol{P}_{k|k-1}^{xy} = \sum_{j=0}^{2L} W_j^{(c)} * \left(\left(\boldsymbol{x}_{k|k-1}\right)_j - \hat{\boldsymbol{x}}_{k|k-1} \right) \left(\left(y_{k|k-1}\right)_j - \hat{y}_k \right) \tag{31}$$

Step5 : Predict the new state vector $\hat{\boldsymbol{x}}_{k|k}$ and covariance matrix $\boldsymbol{P}_{k|k}$

$$\hat{\boldsymbol{x}}_{k|k} = \hat{\boldsymbol{x}}_{k|k-1} + \boldsymbol{K}_k(\bar{y}_k - \hat{y}_k) \tag{32}$$

$$\boldsymbol{P}_{k|k} = \boldsymbol{P}_{k|k-1}^{xx} - \boldsymbol{K}_k \boldsymbol{P}_{k|k-1}^{yy} \boldsymbol{K}_k^T \tag{33}$$

where $\bar{y}_k$ is the measured nonlinear viscous damper force from the experimental substructure. $\hat{\boldsymbol{x}}_{k|k}$ is used at each time step to update the E-NLMM parameters and compute the damper force $f_{d_{k+1}}$ via Eq. (19) for the numerically modelled nonlinear viscous dampers of the analytical substructure.

The online model updating algorithm parameters used herein are based on a measurement noise standard deviation value of 8 kN, and a normalized process noise for the state variables equal to $\sigma N = 0.005$ for the earthquake and $\sigma N = 0.0001$ for the wind RTHS, where $\boldsymbol{Q} = \text{diag}(\sigma N \begin{bmatrix} K_{d_0} & C_{d0} & \alpha_0 \end{bmatrix})^2$. The normalization is performed with respect to the initial value for each state variable $\hat{\boldsymbol{x}}_{k=0|k=0} = \begin{bmatrix} K_{d_0} & C_{d0} & \alpha_0 \end{bmatrix}^T$, with K_{d_0}, C_{d0} and α_0 given in Table 2. The σN values for the normalization process noise were determined from a sensitivity analysis, where they resulted in the smallest normalized RMS error (NRMSE) between the predicted and actual damper force. The measurement noise was established from assessing load cell measurements for at-rest laboratory

conditions of the load cell used to measure the experimental substructure's damper force. The noise covariance matrix $\boldsymbol{Q}$ is based on the assumption that the state variables are uncorrelated, and therefore is a diagonal matrix. It was found that assigning the values for the initial covariance matrix $\boldsymbol{P}_{0|0}$ equal to the initial values for $\boldsymbol{Q}$ produced accurate results. It should be noted that the standard deviation for measurement noise will depend on the load cell used to measure the damper force and the precision of the data acquisition system. Hence, a user should be cautioned to calibrate the value for R for their experimental substructure setup.

The covariance matrix $\boldsymbol{P}_{k-1|k-1}$ must remain semi-positive definite throughout the RTHS, otherwise it will cause the RTHS to terminate since Eq. (23) will result in a complex set of numbers for $\boldsymbol{x}_{k-1|k-1}$. $\boldsymbol{P}_{k-1|k-1}$ is prone to becoming ill conditioned since the value for the state variable for the spring stiffness K_{d_0} is six orders of magnitude larger than the velocity exponent α_0, as noted above. This barrier was overcome by shifting any negative eigenvalues of $\boldsymbol{P}_{k-1|k-1}$ to the eigenvalues of the nearest positive-definite matrix using the procedure of Higham [50]. It was found that round-off error associated with reconstructing a semi-positive-definite matrix form of $\boldsymbol{P}_{k-1|k-1}$ may cause some of the eigenvalues to become negative [51], thereby resulting in $\boldsymbol{P}_{k-1|k-1}$ not being a semi-positive definite matrix. Therefore, any negative eigenvalues of the reconstructed $\boldsymbol{P}_{k-1|k-1}$ were shifted to the positive side of the real-axis by $\varepsilon = 10^{-11}$, where this value for ε for was found by numerical experimentation to be the minimum value to ensure that $\boldsymbol{P}_{k-1|k-1}$ was semi-positive definite. The computer precision of the calculations performed during the RTHS is that associated with a computer with a 64-bit operating system. The procedure to ensure a semi-positive definite covariance matrix $\boldsymbol{P}_{k-1|k-1}$ is given below in Fig. 9, where the resulting $\boldsymbol{P}_{k-1|k-1}$ is used in Eq. (22) of Step 1 presented above. Note that $\boldsymbol{P}_{PSD-C}$ appearing in Fig. 9 is the last semi-positive definite covariance matrix computed, where the initial value for $\boldsymbol{P}_{PSD-C}$ is equal to $\boldsymbol{P}_{0|0}$.

9. RTHS integrated control architecture: description and assessment

The RTHS were performed using the integrated control architecture shown in Fig. 10. It includes a data acquisition system (labeled DAQ), xPC target computer, servo-hydraulic controller, instrumentation and sensors, and SCRAMNet GT. SCRAMNET GT provides reflective memory with a communication speed between the workstations of 90 nsec to enable real-time data sharing. Synchronization is maintained on SCRAMNet GT among the workstations at the real-time control rate of 1024 Hz. The DAQ system has 16-bit precision and acquires data at a

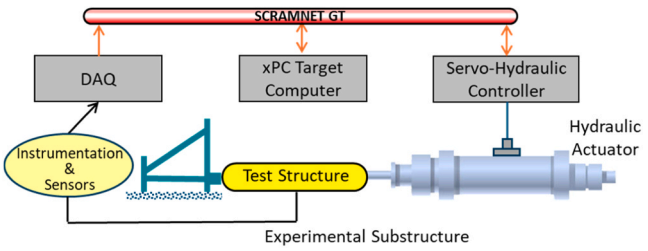

Fig. 10. RTHS integrated control architecture.

scan rate of 4096 Hz. The xPC has a target real-time operating system developed by Mathworks [52] with an Intel Core 3.6 GHz, 8-core CPU and 8 GB of memory. Simulink [52] is used to design a model-in-the-loop system that includes the analytical substructure, on-line model updating algorithm, integration algorithm, and the actuator adaptive compensator that is compiled and loaded onto the xPC. The servo-hydraulic controller is a digital controller that has programmable clock speeds of 1024 Hz and 2048 Hz, where the former was used for the RTHS reported herein. The actuator adaptive compensator functions as an outer loop to the closed loop PID controller that resides on the servo-hydraulic controller. The actuator adaptive compensator receives feedback actuator motion measurement data from the servo-hydraulic controller over SCRAMNet GT, and the compensated actuator commands for the next time step are sent from the xPC target computer back to the servo-hydraulic controller via SCRAMNet GT. The damper load cell readings are acquired by the data acquisition system

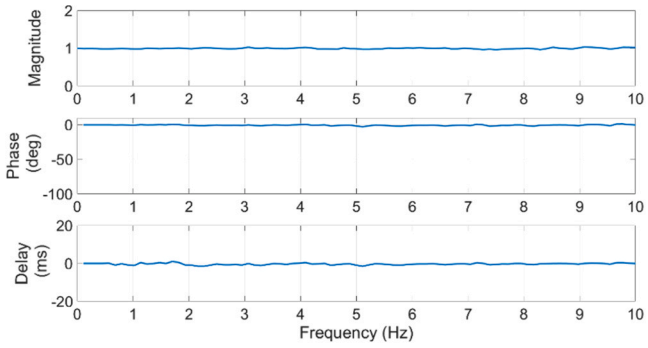

Fig. 11. Transfer system frequency response function from actuator command displacement to measured displacement.

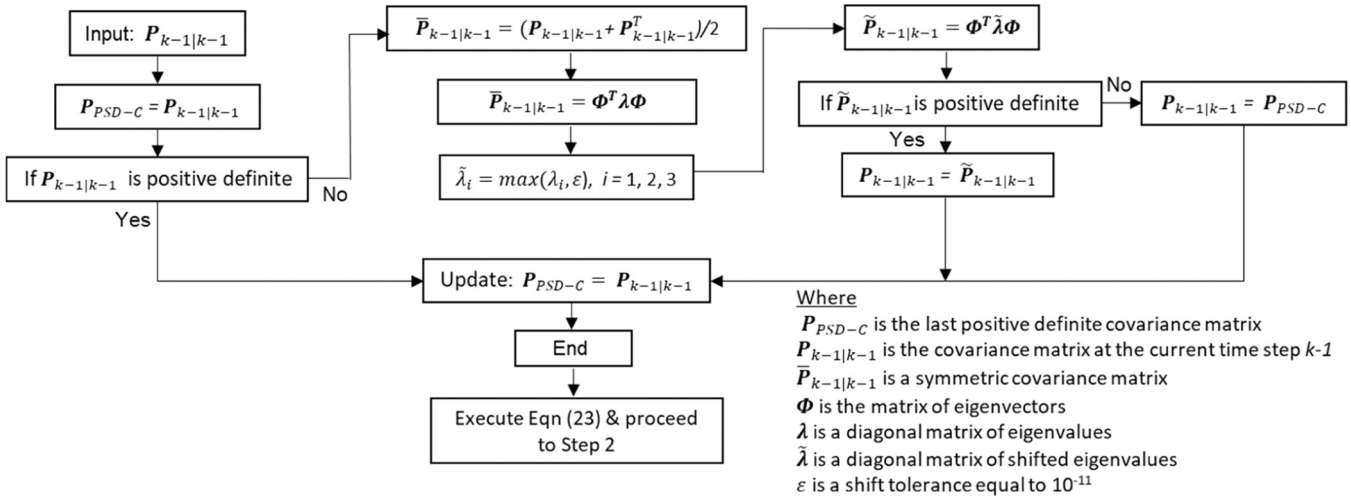

Fig. 9. Procedure to ensure positive definite covariance $\boldsymbol{P}_{k-1|k-1}$ matrix during a RTHS.

and fed by SCRAMNet GT to the xPC target computer, where the on-line model updating algorithm updates the damper model parameters for the numerically modeled dampers of the analytical substructure.

The performance of the transfer system and IT architecture for the RTHS was assessed over a range of frequencies in order to evaluate the dynamic behavior of the experimental substructure and the latency in the integrated control architecture. The assessment involved determining experimentally the frequency response function (FRF) from the actuator target command displacement generated by the xPC target computer to the measured actuator displacement that was fedback to the xPC target computer. The input excitation consisted of band-limited white noise with a frequency range of 0 to 10 Hz and amplitude of 5 mm. Data was recorded at a rate of 1024 Hz over a 45 s duration, and the FRF was calculated using 46080 Fast Fourier Transform (FFT) points with a Hanning windowing with 50 % overlap and 5 averages. The FRF of the system appears in Fig. 11. The FRF has a magnitude in the range of 0.994 to 1.017 with a mean of 0.997 over the frequency range of 0 to 10 Hz. The phase plot was used to establish the time delay in the system as a function of frequency, and is included in Fig. 11. It was found that the average time lag delay over the frequency range of 0 to 10 Hz was 0.24 msec. The delay is considerable smaller than the 11/1024 s time step size and should not affect the RTHS, and for all practical purposes the actuator control is considered to be accurately achieved and in real-time. The natural frequencies of the structure that participated in the response during the RTHS are less than 1 Hz (to be discussed in Section 10), and thus the selection of the frequency range of 0 to 10 Hz for the band-limited white noise test is appropriate. The results for the FRF therefore imply that there is no dynamic resonance from natural frequencies in the experimental substructure's test setup over the 0 to 10 Hz frequency range, that the minimal observed time lag delay in the system implies that no latency exists in the IT architecture, and that exceptional actuator control is expected to be achieved during a RTHS. A further assessment of the adaptive actuator compensation during the RTHS is presented in Section 11.

10. RTHS results

10.1. Building floor displacements and accelerations

The recast integration algorithm, combined with the use of the super element enabled the RTHS of a nonlinear 3D model of the tall building to be successfully completed, where there were no delays observed in completing the algorithm's calculations in real-time. The time history for the roof lateral displacements at the master node are shown in Fig. 12. All results reported in this section are located at the center of floor mass (i.e., the location where the floor mass is lumped at a 5 % eccentricity in both translational directions in the case of the earthquake RTHS, and at the centerline of the floor plan for the wind RTHS). Lateral displacements are reported since they are associated with potential

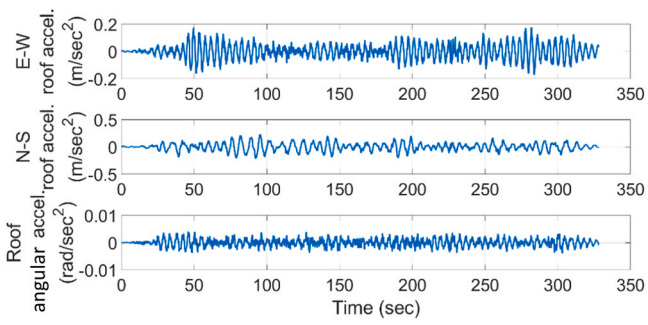

Fig. 13. Roof acceleration during the real-time hybrid simulation under wind load (E-W and N-S accelerations are plotted to different scales for clarity).

structural damage due to story drift and P-Δ effects, and therefore of interest to structural design engineers and researchers. Accelerations developed in tall buildings under wind loading are of concern because they cause discomfort to the occupants and therefore the performance objectives of the building's design are not met. Consequently, roof accelerations developed during the wind RTHS are included in the presentation of the RTHS results, and appear in Fig. 13 at the master node.

The history of roof displacements shown in Fig. 12(a) for the earthquake RTHS shows evidence of residual displacement and twist at the end of the simulation in both the E-W and N-S directions. This residual displacement is caused by inelastic response that developed in the BRBs during the earthquake RTHS, and is discussed later. For the wind RTHS there is no evidence of residual displacements or twist at the end of the time histories plotted in Fig. 12(b), while dynamics oscillations are seen to occur during the simulation. An examination of the element states of the analytical substructure model for the wind RTHS indicated that the structure remained elastic while the dampers exhibited nonlinear behavior during the simulation.

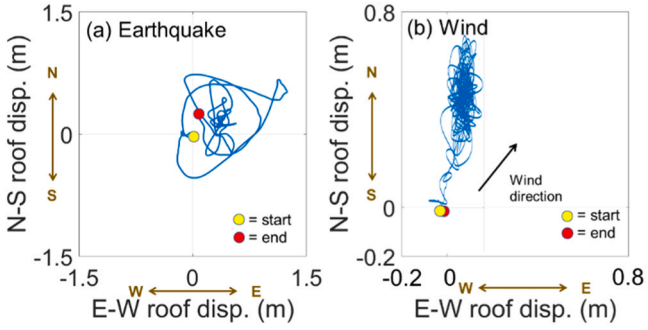

Fig. 14. Roof displacement orbits for (a) earthquake RTHS, and (b) wind RTHS.

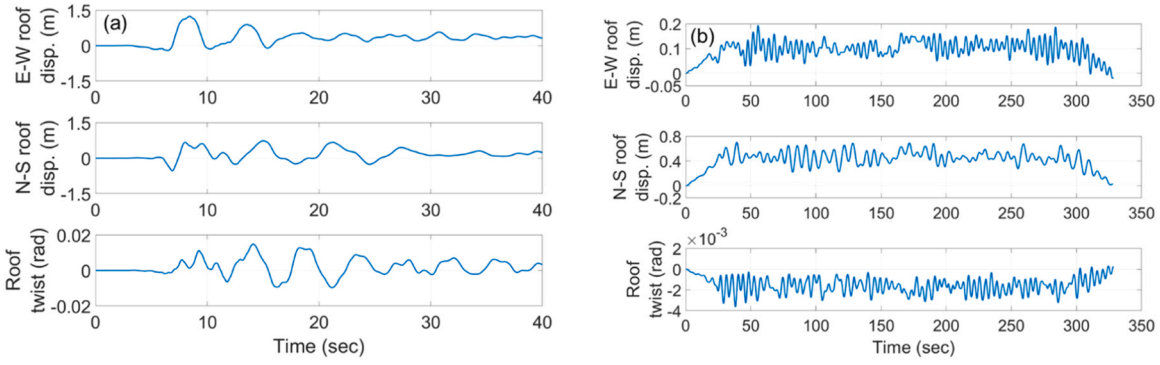

Fig. 12. Roof displacement time histories for (a) earthquake RTHS, and (b) wind RTHS (wind RTHS E-W and N-S displacements are plotted to different scales for clarity).

In addition to the dynamic oscillations from gusts, Fig. 12(b) implies that the building has a static component of displacement and twist occur during the wind RTHS. Due to the load path for the dampers residing in only the N-S direction of the outriggers, the nonlinear viscous dampers contribute to damping the dynamic oscillations in the plane of the outrigger system. They however do not resist the static component of the applied wind loads, that when combined with the lower stiffness in the N-S direction and larger wind exposure results in noticeable higher roof displacements in the N-S direction compared to the E-W direction. The cross wind effects and nonuniform wind gust pressures around the circumference of the building's floor plan are evident in the roof acceleration time histories given in Fig. 13, where there is noticeable roof translational and torsional accelerations that develop in the building during the wind RTHS. The effects of torsional accelerations can lead to greater translational acceleration resultants along the perimeter of the floor plan due to the effect of combined transactional and rotational accelerations at the master node. This phenomenon will be discussed more later.

The orbits of the roof displacement are shown in Fig. 14, where the E-W displacements are plotted against the N-S displacements for the earthquake and wind RTHS. The start and end points for each orbit are noted in the figure. It can be seen that the building does not develop a cyclically symmetric displacement response during the earthquake RTHS where there is a residual roof displacement at the end of the simulation, consistent with the results shown in Fig. 13(a). The static wind drift is apparent in Fig. 14(b) in the direction of the wind (i.e., in the NE direction), in addition to dynamic oscillations caused by the cross-wind effect and gust during the wind RTHS. Additionally, there is no residual roof displacement at the end of the wind RTHS, indicating elastic response of the structural system under wind.

The peak story displacements along the height of the building are shown in Fig. 15 for the earthquake and wind RTHS. The peak story displacements are larger in the E-W direction compared to the N-S direction over the height of the building under the earthquake, but are vise-versa under the wind RTHS. As noted above, the dampers in the building do not have the ability to resist the static component of the wind, and when combined with a larger wind exposure and lower lateral stiffness in the N-S direction, leads to a larger displacement in the N-S direction compared to the E-W direction under the wind loading. Under the earthquake loading, the damped outriggers contribute to reducing the motions in the N-S direction. Twist occurs over the height of the building during both the earthquake RTHS and the wind RTHS.

10.2. Buckling restrained brace response

As noted above in the earthquake RTHS, only the BRBs developed inelastic response. Shown in Fig. 16 are the axial force-deformation hysteretic responses of selected BRB's at the 8th story. The 8th story is the location where the maximum BRB ductility demand occurred in the structure in the N-S (BRBF 1) and E-W (BRBF 3) directions. All of the remaining members except for the BRBs had deformations that were less than their yield deformations, and hence modeling them as linear elastic members is justified. For the wind RTHS, all of the members including the BRBs remained elastic. The peak BRB ductility over the height of the building is shown in Fig. 17 for BRBFs identified as 1, 2, 3, and 4 in the building's floor plan given in Fig. 1(b). BRBFs 1 and 2 are in the column line at the west and east ends of the floor plan and are part of the outrigger systems that resist lateral loads in the N-S direction. These two BRBFs have the furthest distance of all of the BRBFs from the center of rigidity of the building's floor plan (located at the center of the floor plan since the building is symmetric in plan), and hence are most susceptible to torsional effects. The torsional demand led to a difference in the ductility demand of these two BRBFs, as seen in Fig. 17(a). The ductility demand is higher in the E-W direction (Fig. 17(b)) compared to the N-S direction (Fig. 17(a)), and is explained by the fact that the spectral accelerations are larger in the E-W direction, as noted previously, where the fundamental period is $T_1^{EW} = 4.07$ s compared to $T_1^{EW} = 6.71$ s in the N-S direction (see Fig. 4(c)). The ductility demand in BRBFs 3 and 4, which resist lateral load in the E-W direction, also differ because of torsional effects.

The peak floor translational and angular accelerations along the height of the building from the wind RTHS are shown in Fig. 18. The results in Fig. 18(a) and (b) are associated with the center of gravity of the building (i.e., center of the floor plan for the wind loading RTHS), and Fig. 18(c) compares the maximum acceleration resultant at the center of the floor plan with the maximum resultant among the four corners of the building. The peak floor accelerations at the 20th, 30th, and 40th floors are tabulated in Table 3, where they are compared to the peak magnitude of the floor acceleration resultant among the four corners of the building.

10.3. Effect of building twist on peak floor wind accelerations

The resultant of the peak accelerations among all of the corners of the building in Fig. 18(c) and Table 3 are shown to be greater than that at the center of the floor plan (marked as c.g. in Fig. 18(c)). The increase in

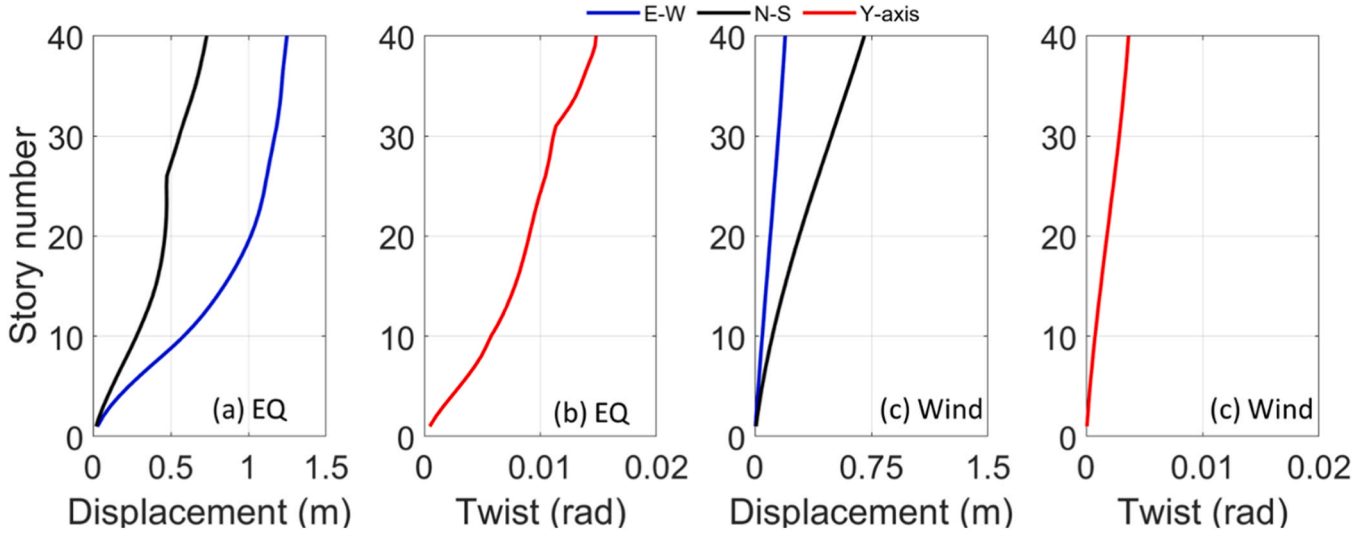

Fig. 15. Peak floor displacement along height of building: (a) peak displacement in N-S and E-W directions under earthquake; (b) peak twist about Y-axis under earthquake; (c) peak floor displacement in N-S and E-W directions under wind; and, (d) peak floor twist about the Y-axis under wind.

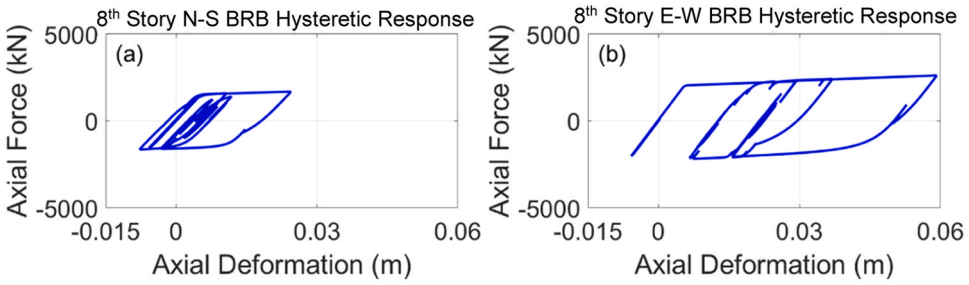

Fig. 16. BRB force-deformation response under earthquake RTHS in (a) N-S and (b) E-W directions in BRBFs 1 and 3 identified in Fig. 1(b).

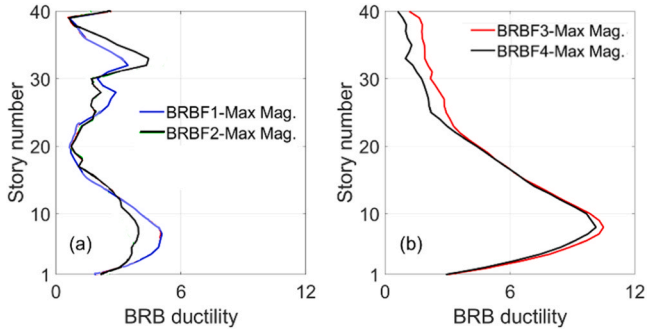

Fig. 17. Peak magnitude of BRBF ductility over the height of the building in the (a) N-S and (b) E-W directions of selected BRBFs 1, 2, 3, and 4 (see Fig. 1(b) for BRBF floor plan layout).

the acceleration resultant at the corners of the building is shown in Fig. 18(d). The increase in acceleration at the corners of the floor plan is associated with multi-axis response where the angular and translational accelerations develop in the structure. This indicates the need to consider a 3-D model and account for angular accelerations in determining the resultant translational accelerations throughout the floor plan and over the height of a building, since the results at the center of gravity and at the corners of the floor plan can have a considerable difference. For example, Table 3 shows the peak acceleration resultant increase by 18.2 % from 24.1 milli-g at the center of the floor to 28.5 milli-g at the corner of the 40th floor, whereas this increase is 47.4 % at the 20th floor. Note that large percent increases near the ground floor level are associated with a small acceleration resultant at the center of gravity, and are not as meaningful as that in the upper floors.

10.4. Nonlinear viscous damper response

The measured force-deformation response of the experimental substructure's damper under the earthquake and wind RTHS is shown in Fig. 19 for one damper (labeled *Measured*). As noted previously, the experimental damper corresponds to the NW corner of the 30th story during the earthquake RTHS and the NE corner of the 30th story during the wind RTHS (see Fig. 3). The results are plotted using a different set of scales in order to better illustrate the damper's response for the earthquake and wind RTHS. The damper force-velocity response is given in Fig. 20 for the earthquake and wind RTHS. The results in Fig. 20(a) and (b) are plotted using a different set of scales in order to better illustrate the damper's response for the earthquake and wind RTHS. The damper response under earthquake loading in Figs. 19 and 20 show a capping of its force which occurs at the larger velocities and is characteristic of nonlinear viscous dampers. In addition, the damper force-deformation hysteretic response from the earthquake RTHS is more centered about the origin than the response under wind. The response under wind has a

Table 3
Peak of resultant floor acceleration at the center and corner of floor plan, respectively.

Case	Peak floor acceleration (milli-g)		
	20th floor	30th floor	40th floor
c.g.	11.8	19.3	24.1
Corner	17.4	23.0	28.5
Increase (%)	47.4	19.1	18.2

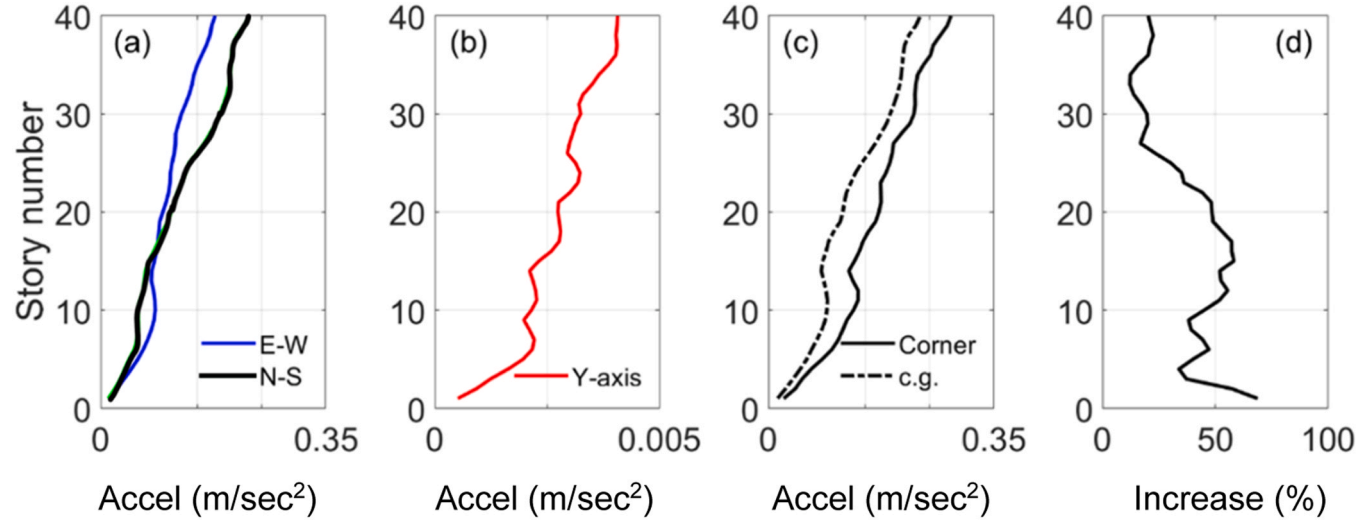

Fig. 18. Wind RTHS: (a), (b) peak floor accelerations over height of the building; (c) peak resultant accelerations at center and corner of floor plan; and (d) acceleration resultant increase at corners of floor plan.

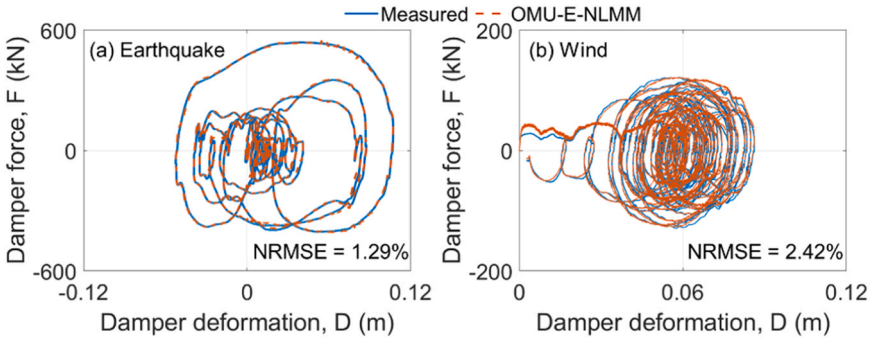

Fig. 19. Force-displacement response of experimental damper: (a) earthquake RTHS; and (b) wind RTHS (note: earthquake and wind RTHS results are plotted at different scales).

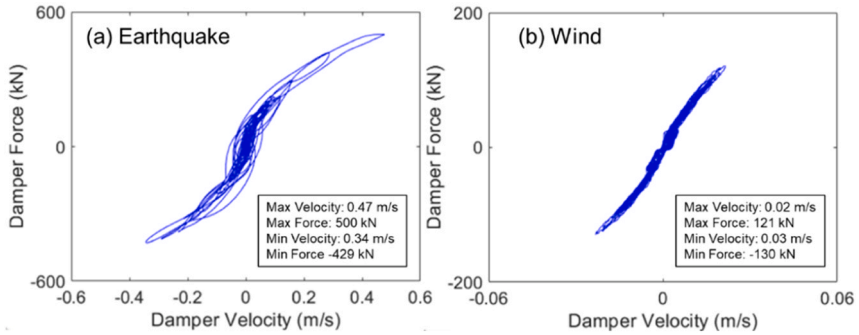

Fig. 20. Force-velocity response of experimental damper: (a) earthquake RTHS; and (b) wind RTHS (note: earthquake and wind RTHS results are plotted at different scales).

lower level of force due to smaller velocities that develop in the damper, where the damper appears to respond more like a linear viscous damper having elliptical-like shaped hysteresis loops in Fig. 19(b) and a fairly linear trend in the force-velocity response shown in Fig. 20(b). The drift in the damper deformation in Fig. 19(b) is associated with the static component of the wind loading during the ramping up of the wind loading, about which the damper's motion oscillates under the gust loading before returning towards the origin during the ramping down of the wind loading.

The *Measured* results are compared to the force prediction for the experimental substructure damper force in Fig. 19(a) and (b) using the updated values for the model parameters $\hat{\mathbf{x}}_{k|k}$ from Eq. (32) of the OMU-E-NLMM algorithm, where the RMSE between the measured results and predicted (i.e., OMU-E-NLMM) is 1.29 % and 2.42 % for the earthquake and wind RTHS, respectively. These NMRSE values and the plotted hysteretic response shown in Fig. 19(a) and (b) exhibit excellent agreement between the measured damper force and the predicted damper force of the experimental substructure for both the earthquake and wind RTHS. Further discussion about the accuracy of the OMU-E-NLMM is given later related to the other dampers that were numerically modeled in the building.

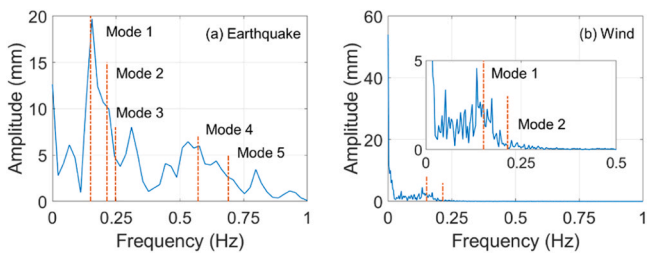

Fig. 21. Frequency decomposition of measured damper deformation in experimental substructure during the RTHS: (a) earthquake; and(b) wind.

Table 4
Modal frequencies from linear eigenvalue analysis.

RTHS building model	Modal frequency, f (Hz)				
	Mode 1	Mode 2	Mode 3	Mode 4	Mode 5
Earthquake	0.149	0.213	0.246	0.570	0.685
Wind	0.150	0.214	0.241	0.585	0.683

The frequency decomposition of the damper measured deformations is shown in Fig. 21. The damper deformations are those measured in the experimental substructure. It is evident from the peaks in the Fourier amplitudes in this figure that there is a greater amount of higher frequency content in the damper deformation response for the earthquake RTHS compared to the wind RTHS. Under both the earthquake and wind RTHS there is an appreciable amount of response with a frequency close to zero. For the earthquake RTHS this is due to the inelastic response that occurred in the structure that led to a gradual drifting in the deformations of the damper from the initial position associated with the residual drift in the building. For the wind RTHS this is associated with the static component of drift that occurs in the damper, where there is oscillation about an offset as discussed previously, see Fig. 19(b).

A summary of the first-five modal frequencies for the building from a linear eigenvalue analysis is given in Table 4. To perform the eigenvalue analysis, it was necessary to linearize the nonlinear viscous dampers using the procedure described in Al-Subaihawi [42] and Kolay and Ricles [32]. Modes 1 through 5 of the earthquake RTHS building model with an eccentric mass are: (1) first translational mode in the N-S direction combined with torsion and associated with the natural period T_1^{NS}; (2) first predominantly torsional mode; (3) first translational mode in the E-W direction combined with torsion and associated with the natural period T_1^{EW}; (4) second translational mode in the N-S direction

combined with torsion; and (5) second translational mode in the E-W direction combined with torsion. For the wind RTHS building model with a concentric mass modes 1 through 5 are: (1) first translational mode in the N-S direction; (2) first torsional mode; (3) first translational mode in the E-W direction; (4) second translational mode in the N-S direction; and (5) second translational mode in the E-W direction combined with torsion. Table 4 indicates that the modal frequencies of the two models are similar. These frequencies are identified in Fig. 21. The values are not precise frequencies of modal vibration since in the earthquake RTHS the structure developed inelastic response. In addition, both for the earthquake and wind models the dampers are linearized at the fundamental natural frequency of the building. While the modal frequencies are not precise values, their position in Fig. 21 gives some indication of which modes likely contributed to the deformation history of the physical damper positioned on the 30th story at the NW corner (earthquake RTHS) and the NE corner (wind RTHS). Modes 1 through 5 all appear to have contributed to the damper deformations during the earthquake RTHS. The warping torsion mentioned previously results in torsional motions of the building creating deformations in the dampers, and hence all of these modes contribute. For the wind RTHS, where there is no coupling between torsion and translation due to the concentric placement of the floor mass in the wind RTHS model, and damper deformations appear to be primarily associated with the first mode.

11. RTHS actuator control assessment

As mentioned previously, the ATS compensator developed by Chae et al. [25] is used to compensate for actuator time delay and amplitude error. The settings for the ATS coefficients in the RTHS involving the two natural hazards are tabulated in Table 1 and based on the recommendations of Kolay et al. [34] for 2D RTHS. The ATS modifies the command displacement to the actuator in order to reduce both the amplitude and delay errors that are inherent in the servo-hydraulic system. The synchronized subspace plots of the target and measured displacements of the experimental damper during the RTHS are shown in Fig. 22(a) and (b). The plots show a slope close to 45 degrees with minimal hysteresis, where the NRMSE is 0.13 % and 0.04 % during the earthquake and wind RTHS, respectively. These results indicate accurate actuator control was achieved during the RTHS.

The time histories of the ATS adaptive coefficients for the actuator are shown in Fig. 22(c) and (d) for the earthquake and wind RTHS. The values of the coefficients give an indication of the correction that took place for actuator amplitude error A_k and delay compensation τ_k at each time step k of the RTHS, where

$$A_k = \frac{1}{a_{0,k}}, \quad \tau_k = \frac{a_{1,k}}{a_{0,k}} \tag{34a, b}$$

The results in Fig. 22(c) show that A_k ranged from 0.98 to 1.02 in the earthquake RTHS. The value for a_0 was fixed at 1.0 for the wind RTHS since no amplitude error was found to occur and therefore no compensation for amplitude error was necessary, see Fig. 22(d). The compensated delay $\tau_k$was found to range from 13 msec to 25 msec for the earthquake RTHS (Fig. 22(c)) and from 9 msec to 27 msec for the wind RTHS (Fig. 22(d). The amount of compensated delay exceeds the time step of 11/1024 s, and without the use of the adaptive compensation the RTHS results would have been unreliable and the test potentially unstable since delay introduces negative damping into an integration algorithm [34]. The actual delay that was found in the RTHS by comparing the histories of measured against targeted actuator displacement had a maximum value of 1 msec, which is close to the average time lag delay of 0.24 msec calculated from the phase plot in Section 9.

The damper velocity-damper force relationship for the earthquake and wind RTHS were shown previously in Fig. 20. In Fig. 20 the earthquake RTHS is seen to impose larger forces and velocities on the damper than that for the wind RTHS. Additionally, the damper is seen to develop a greater degree of nonlinearity in the force-velocity during the earthquake RTHS compared to the wind RTHS. Consequently, the ATS compensator was required to exert more effort in the actuator tracking due to the greater extent of dynamic interaction between the hydraulic actuator and nonlinear viscous damper during the earthquake RTHS. This is reflected in the fact that the coefficients for displacement $a_{0,k}$ and acceleration $a_{2,k}$ in the ATS compensator algorithm (see Eq. (17)) were required to undergo continuous change and the history of the value for the coefficient for velocity $a_{1,k}$ in Fig. 22 shows a greater variation during the earthquake RTHS compared to the wind RTHS in order to maintain accurate control of the actuator.

12. Nonlinear viscous damper on-line model updating assessment

The histories of the adaptation of the damper model parameters K_d, C_d, and α that were identified by the OMU-E-NLMM algorithm during the earthquake RTHS and wind RTHS are shown in Fig. 23. These results represent the histories of the updated model parameters associated with the state vector $\hat{\mathbf{x}}_{k|k}$ determined by Eq. (32) that were used in the remaining numerically modeled dampers throughout the building. The values for K_{d0}, C_{d0}, and α are normalized by their initial values (K_{d0}, C_{d0}, α_0) in Fig. 23, and are shown to vary from their initial values over the course of the RTHS. There is a different trend in the variation of the coefficients for the earthquake compared to the wind RTHS. With the exception of K_d, there is a greater variation in the values of the coefficients C_d and α from their initial values for the earthquake RTHS compared to the wind RTHS.

It was found that the online model updating procedure failed if the procedure given in Fig. 9 was not used which ensured that the covariance matrix for the state variables, $\boldsymbol{P}_{k|k}$, remained positive definite. Consequently, the real-time hybrid simulation had to be terminated

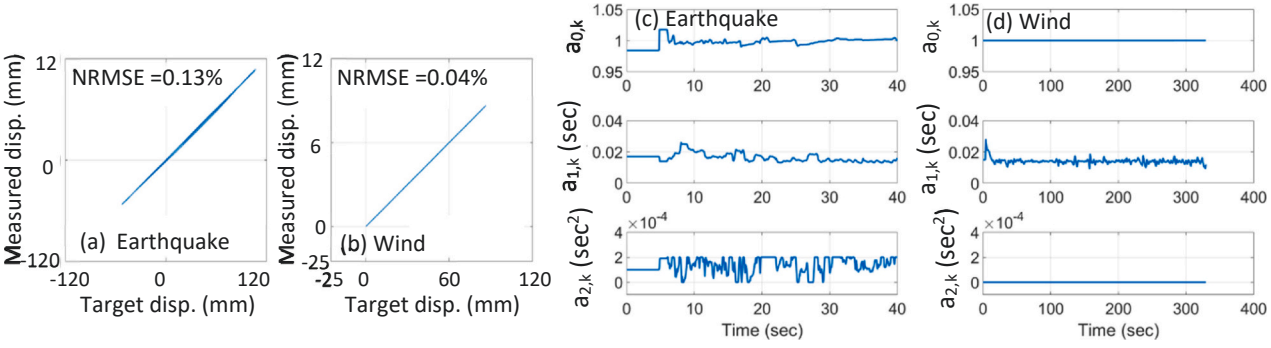

Fig. 22. Synchronized subspace plots of target and measured actuator displacements for (a) earthquake RTHS and (b) wind RTHS; time history of ATS coefficients for (c) earthquake RTHS and (d) wind RTHS.

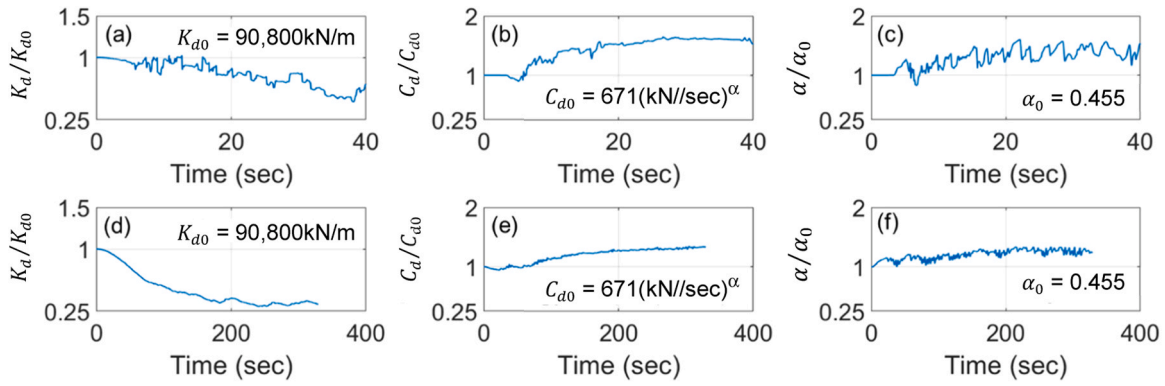

Fig. 23. Identified damper model parameters during earthquake RTHS (a, b, and c); wind RTHS (d, e, and f).

Table 5
NRMSE between RTHS and Post RTHS Measured damper forces.

Hazard	Damper Force NRMSE Error (%)											
	40 NW	40 NE	40 SW	40 SE	30 NW	30 NE	30 SW	30 SE	20 NW	20 NE	20 SW	20 SE
EQ	2.20	4.60	2.63	3.22	-	2.30	1.55	2.37	2.19	3.29	2.25	3.26
Wind	2.81	2.36	2.47	2.63	2.69	-	2.77	2.51	3.21	3.26	3.10	3.26

prematurely.

Following the completion of the RTHS the damper deformation history from the RTHS of each numerically modeled damper was imposed onto the physical damper in the experimental substructure and the damper force was measured. The former is referred to as the *RTHS* and the latter as the *Post RTHS Measured* damper forces. The NRMSE was then computed based on the error between the *RTHS* and the *Post RTHS Measured* damper forces. The comparison enables an assessment of the accuracy of the online model updating algorithm (OMU-E-NLMM) in predicting the force response of the numerically modeled dampers throughout the building during a RTHS. The results are shown in Table 5, where the location of the dampers is identified by the story and corner of the building of the floor plan (see Fig. 3).

The results in Table 5 have an NRMSE between the *RTHS* and *Post RTHS Measured* damper forces that ranges from 1.55 % (30th story, SW corner) to 4.60 % (40th story, NE corner) for the earthquake RTHS, and from 2.36 % (40th story, NE corner) to 3.26 % (20th story, NE and SE corners) for the wind RTHS. The earthquake RTHS has a higher NRMSE among the dampers compared to the wind RTHS, and is explained by the fact that in the earthquake RTHS there is a greater velocity and deformation demand imposed on the dampers and therefore larger force output which leads to larger error in the OMU-E-NLMM based predicted force. In addition, there is a greater degree of higher mode participation in the damper deformation during the earthquake RTHS, as discussed before (see Fig. 21), where the dampers are not completely in phase. This effects the accuracy in applying updated model parameters to dampers that have a different velocity than the experimental substructure's damper. The forces developed in the dampers during the earthquake RTHS were as much as five times larger than that during the wind RTHS (e.g., see Fig. 19). Nonetheless, the *RTHS* hysteretic response appears to agree well with the *Post RTHS Measured* response for each damper, implying that the OMU-E-NLMM algorithm enabled a reasonable prediction to be made of the damper behavior in the numerically modeled dampers throughout the building during the RTHS.

The Post RTHS damper forces are compared in Table 6 with the damper forces predicted using constant parameters values of $\widehat{\mathbf{x}}_{k=0|k=0}$ in the E-NLMM, where the latter is referred to as *RHTS Constant Parameters*. The *RHTS Constant Parameters* damper forces are computed using the damper deformations from the RTHS applied to the E-NLMM. When comparing the results in Table 6 to those in Table 5, it is apparent that there is an increase in the NRMSE for the damper force when constant parameters are used to model the nonlinear viscous dampers, more notably for the wind RTHS.

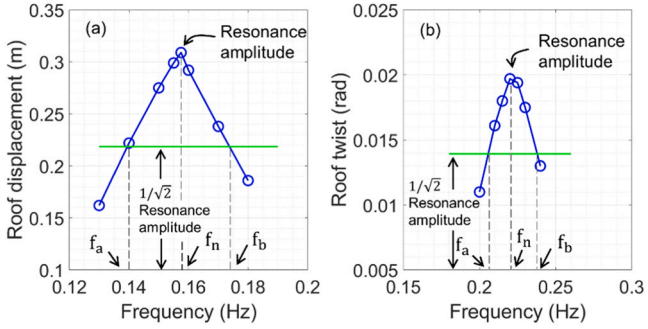

Fig. 24. Steady state response of the building during RTHS half-power method tests: a) steady state roof displacement in N-S direction; and, b) steady state roof twist about the Y-axis.

Table 6
NRMSE between RTHS Constant Parameters and Post RTHS Measured damper forces.

Hazard	Damper Force NRMSE Error (%)											
	40 NW	40 NE	40 SW	40 SE	30 NW	30 NE	30 SW	30 SE	20 NW	20 NE	20 SW	20 SE
EQ	3.45	4.28	2.97	3.23	2.85	2.78	2.57	2.85	2.85	3.46	2.96	3.13
Wind	7.08	7.39	6.81	7.56	7.30	7.02	7.15	6.78	7.23	7.66	7.49	7.70

13. Measurement of system equivalent supplemental viscous damping

Additional RTHS were performed to experimentally determine the amount of supplemental viscous damping provided by the dampers using the half-power bandwidth method (HPB) [53]. In these RTHS the model of the building for the wind RTHS was subjected to constant amplitude hormonic loading at the center of the roof floor plan at multiple frequencies around the anticipated damped natural frequency of the system. A translational load was applied in the N-S direction to excite the first mode and a torsional load about the Y-axis to excite the second mode. The load is of small amplitude in order to keep the building elastic. The floor mass was not assigned any eccentricity in the HBP tests, and three parallel dampers were placed between each outrigger truss and perimeter column as shown in Fig. 3(c) to be consistent with the wind RTHS results. Hence, the amount of equivalent damping is associated with the structure in the wind RTHS. The cyclic loading for the HPB RTHS included two ramping up cycles, ten cycles with constant amplitude, and three ramping down cycles. The peak displacement amplitude of the damper during the RTHS HPB tests was around 25 mm to match the amplitude of damper oscillations from the offset observed during the wind RTHS, as shown in Fig. 19(b).

The steady state amplitude of roof displacement and twist are shown in Fig. 24. Only the translation in the N-S direction (Fig. 24(a)), and twist about the Y-axis (Fig. 24(b)) are considered, which as explained in Section 2 of the paper the orientation of the outrigger trusses and load paths to the BRBFs leads to minimal damper deformation under loading in the E-W direction, and therefore RTHS with E-W loading are excluded from the HPB tests. An examination of the mode shapes of the model revealed that axial deformations develop in the dampers for modes with torsional motions, where this phenomenon is associated with warping torsion discussed previously in Section 10. The measured damping for the first translational mode in the N-S direction $\xi_{1,N-S}$ was found to be 10.4 %, and for the first torsional mode about the Y-axis $\xi_{1,Y-Y}$ was 7.5 %. The damping is estimated from Fig. 24 using $\xi = (f_b - f_a)/2f_n$, where f_b and f_a are the two frequencies that intersect the HPB curve at $1/\sqrt{2}$ the resonance amplitude, and f_n is the resonance frequency [53]. The resonance frequencies were found to be 0.157 Hz and 0.214 Hz and represent the respective frequencies for the first-two modes for the wind RTHS building model. These measured values are close to that from the linear eigenvalue analysis results reported in Table 4 for the wind RTHS building model. Recall that the analytical substructure included 2 % inherent modal damping for modes 1 through 30, therefore the identified damping for $\xi_{1,N-S}$ and $\xi_{1,Y-Y}$ are reduced by 2 %, leading to the supplemental damping ratios of 8.4 % and 5.5 % for the first translational and torsional modes, respectively, associated with adding the dampers to the system.

14. Summary and conclusions

A framework for performing 3-D RTHS of a tall building based on a reformulated MKR-α explicit unconditionally stable integration algorithm is presented and used to conduct simulations. The analytical substructure consisted of a 3-D nonlinear model of the building while the experimental substructure consisted of a full-scale nonlinear viscous damper. The remaining dampers in the building are modeled using an explicit-based non-iterative nonlinear Maxwell model with a real-time online model updating approach. Due to significant differences in the order of magnitude of the model parameters, the covariance matrix for the state variables is prone to becoming ill-conditioned, which will cause a RTHS to become unstable and be terminated. Therefore, a newly developed stabilized formulation of the constrained unscented Kalman filter is presented and used to perform the real-time online model updating of the damper model's parameters. A super element formulation was developed and used to reduce the number of degrees of freedom of the analytical substructure through static condensation. Selected degrees of freedom that were condensed are associated with elements known to remain elastic during the RTHS. These elements include the columns and beams of the BRBFs. Rigid floor diaphragms are modeled using a master-slave constraint at each floor to account for multi-axis motions of the building under multi-directional loading. An adaptive actuator controller is used to achieve accurate displacements of the experimental substructure's actuator.

The recast integration algorithm, combined with the use of the super element enabled the RTHS of a nonlinear 3D model of the tall building to be successfully completed, where there were no delays in completing the algorithm's calculations in real-time. The online model updating formulation with an explicit form of the nonlinear Maxwell model was able to provide reasonable predictions of the damper hysteretic behavior, showing improved results compared to predictions based on a model with constant damper model parameters. The trend in adaptation of the algorithm's coefficients differs in the earthquake RTHS compared to the wind RTHS. This phenomenon is due to the greater amount of specimen-actuator interaction that takes place in the earthquake simulations that is associated with the larger velocities imposed onto the damper and the greater forces developed in the damper.

The RTHS results demonstrate the importance of using 3-D models to capture multi-directional multi-axis behavior, where under wind loading the differential pressure that develops around the building's circumference and cross-wind effects can generate angular accelerations that increase the translational accelerations at the corners of the floor plan. Under earthquake loading, bi-directional ground motions as well as an eccentricity in the floor plan between the center of mass and the center of rigidity results in a multi-axis response of combined translation with torsional motions of the building. This leads to differences in the story drift of individual RRBS. Consequently, the ductility demand can vary among BRBFs that are orientated in the same direction of the floor plan. Motions that are orthogonal to the plane of the outriggers did not engage the dampers because of the load path of the outrigger system, and thus the dampers are not effective in reducing motions in this direction. However, a warping torsion effect occurs, where deformations in the dampers develop when the building is subjected to torsional loading. Hence, the damped outrigger system also provided damping to torsional modes of vibration of the building. RTHS was found to be an effective means to perform a half-power bandwidth test to assess the amount of supplemental damping that is added to the building system from the dampers. The supplemental viscous damping in the building was found to be 8.4 % and 5.5 % for the first translation and torsional modes, respectively, of the wind RTHS model.

The framework and algorithms presented herein provide tools to experimentally investigate the 3D performance of tall buildings with rate dependent response modification devices that are subjected to multi-natural hazards.

Author statement

The authors do not have any financial or personal relationships with other people or organizations that could in appropriately influence the work reported in the manuscript. The manuscript has not been published previously nor has it been submitted to any other journal for review for publication. All of the authors approve of the publication, and that, if accepted, the manuscript will not be published elsewhere in the same form.

CRediT authorship contribution statement

Safwan Al-Subaihawi: Writing – original draft, Investigation, Formal analysis. **Thomas Marullo:** Visualization, Validation, Software, Data curation. **Spencer Quiel:** Writing – review & editing. **James Ricles:** Writing – review & editing, Supervision, Project administration, Methodology, Funding acquisition, Conceptualization.

Declaration of Competing Interest

None.

Data availability

Data will be made available on request.

Acknowledgements

This research was performed at the NHERI Lehigh Experimental Facility, whose operation is supported by a grant from the National Science Foundation (NSF) under Cooperative Agreement No. CMMI-2037771. This material is based upon the research supported by the NSF under Grant No. 1463497 and support from MTS Corporation. The support by NSF and MTS is gratefully acknowledged. Many thanks to Taylor Devices, Inc. for providing the nonlinear fluid viscous damper used in this research. The opinions, findings, conclusions and recommendations expressed herein are those of the authors and do not necessarily reflect the views of the National Science Foundation or the other sponsors. Data from this study is available upon request.

References

[1] Mahin S, Shing P. Pseudodynamic method for seismic testing. J Struct Engr 1985; 111(7):1482–503. https://doi.org/10.1061/(ASCE)0733-9445(1985)111:7(1482).
[2] Nakashima M, Kato H, Takaoka E. Development of real-time pseudo dynamic testing. Earth Engr Struct Dyn 1992;21(1):79–92. https://doi.org/10.1002/eqe.4290210106.
[3] Shing P., Mahin S. Pseudodynamic test method for seismic performance evaluation: theory and implementation. Earthquake Engineering Research Center, University of California, Berkeley. Report No. UCB/EERC-84/01.
[4] Smith R, Merello R, Willford M. Intrinsic and supplementary damping in tall buildings. Proc Inst Civ Eng-Struct Build 2010;163(SB2):111–8. https://doi.org/10.1680/stbu.2010.163.2.111.
[5] Smith R, Willford M. The damped outrigger concept for tall buildings. Struct desn Tall Spec bldgs 2007;16(4):501–17. https://doi.org/10.1002/tal.413.
[6] Fang C, Spencer Jr B, Xu J, Tan P, Zhou F. Optimization of damped outrigger systems subject to stochastic excitation. Engr Struct 2019;191:280–91. https://doi.org/10.1016/j.engstruct.2019.04.011.
[7] Tan P, Fang C, Zhou F. Dynamic characteristics of a novel damped outrigger system. Earth Engr Engr Vibr 2014;13:293–304. https://doi.org/10.1007/s11803-014-0231-3.
[8] Nagarajaiah S, Chen L, Wang M. Adaptive stiffness structures with dampers: seismic and wind response reduction using passive negative stiffness and inerter systems. J Struct Eng 2022;148(11):04022179. https://doi.org/10.1061/(ASCE)ST.1943-541X.0003472.
[9] Wang M, Nagarajaiah S, Sun F. A novel crosswind mitigation strategy for tall buildings using negative stiffness damped outrigger systems. Struct Ctrl Health Monit 2022;29(9):e2988. https://doi.org/10.1002/stc.2988.
[10] Xing L, Gardoni P, Zhou Y, Aguaguiña M. Optimal outrigger locations and damping parameters for single-outrigger systems considering earthquake and wind excitations. Engr Struct 2021;245:112868. https://doi.org/10.1016/j.engstruct.2021.112868.
[11] Malik F, Kolay C. Optimal parameters for tall buildings with a single viscously damped outrigger considering earthquake and wind loads. Struct desgn Tall Spec bldgs 2023;32(7):e2003. https://doi.org/10.1002/tal.2003.
[12] Al-Subaihawi S, Ricles J, Quiel S. Online explicit model updating of nonlinear viscous dampers for real time hybrid simulation. Soil Dyn Earth Engr 2022;154:107108. https://doi.org/10.1016/j.soildyn.2021.107108.
[13] Al-Subaihawi S, Kolay C, Marullo T, Ricles J, Quiel S. Assessment of wind-induced vibration mitigation in a tall building with damped outriggers using real-time hybrid simulations. Engr Struct 2020;205:110044. https://doi.org/10.1016/j.engstruct.2019.110044.
[14] Dong B, Sause R, Ricles J. Accurate real-time hybrid earthquake simulations on large-scale MDOF steel structure with nonlinear viscous dampers. Earth Engr Struct Dyn 2015;44(12):2035–55. https://doi.org/10.1002/eqe.2572.
[15] Dong B, Sause R, Ricles J. Seismic response and performance of a steel MRF building with nonlinear viscous dampers under DBE and MCE. J Struct Engr 2016;142(6):04016023. https://doi.org/10.1061/(ASCE)ST.1943-541X.0001482.
[16] Chen C, Ricles J, Marullo T, Mercan O. Real-time hybrid testing using the unconditionally stable explicit CR integration algorithm. Earth Engr Struct Dyn 2009;38(1):23–44. https://doi.org/10.1002/eqe.838.
[17] Karavasilis T, Ricles J, Sause R, Chen C. Experimental evaluation of the seismic performance of steel MRFs with compressed elastomer dampers using large-scale real-time hybrid simulation. Eng Struct 2011;33(6):1859–69. https://doi.org/10.1016/j.engstruct.2011.01.032.
[18] Asai T, Chang C-M, Phillips BM, Spencer Jr BF. Real-time hybrid simulation of a smart outrigger damping system for high-rise buildings. Eng Struct 2013;57:177–88. https://doi.org/10.1016/j.engstruct.2013.09.016.
[19] Fermandois GA, Spencer BF. Model-based framework for multi-axial real-time hybrid simulation testing. Earthq Eng Eng Vib 2017;16(4):671–91. https://doi.org/10.1007/s11803-017-0407-8.
[20] Najafi A, Fermandois GA, Spencer Jr BF. Decoupled model-based real-time hybrid simulation with multi-axial load and boundary condition boxes. Eng Struct 2020;219(Sep):110868. https://doi.org/10.1016/j.engstruct.2020.110868.
[21] Najafi A, Spencer Jr BF. Multiaxial real-time hybrid simulation for substructuring with multiple boundary points. . (November 2021) J Struct Eng 2021;147(11):05021007. https://doi.org/10.1061/(ASCE)ST.1943-541X.0003138.
[22] Shao X, Mueller A, Mohammed BA. Real-time hybrid simulation with online model updating: methodology and implementation. J Eng Mech 2015;142(2):04015074.
[23] Ou G, Dyke SJ, Prakash A. Real time hybrid simulation with online model updating: an analysis of accuracy. Mech Syst Signal Process 2017;84:223–40.
[24] Song W, Hayati S, Zhou S. Real-time model updating for magnetorheological damper identification: an experimental study. Smart Struct Syst 2017;20(5):619–36.
[25] Chae Y, Kazemibidokhti K, Ricles J. Adaptive time series compensator for delay compensation of servo-hydraulic actuator systems for real-time hybrid simulation. Earth Engr Struct Dyn 2013;42(11):1697–715. https://doi.org/10.1002/eqe.2294.
[26] Moehle et al. Case studies of the seismic performance of tall buildings designed by alternative means. Pacific Earthquake Engineering Research Center, University of California, Berkeley, California; 2011 July. Report No.: PEER 2011/5.
[27] Moehle et al. Final report to the city of Los Angeles for the tall building initiative. Pacific Earthquake Engineering Research Center, University of California, Berkeley; 2009.
[28] ASCE 7-05. Minimum design loads for buildings and other structures. (USA): American Society of Civil Engineers; 2005. https://doi.org/10.1061/9780784408094.
[29] Kolay C, Ricles J. Improved explicit integration algorithms for structural dynamic analysis with unconditional stability and controllable numerical dissipation. J Earth Engr 2019;23(5):771–92. https://doi.org/10.1080/13632469.2017.1326423.
[30] Kolay C, Ricles J, Marullo T, Mahvashmohammadi A, Sause R. Implementation and application of the unconditionally stable explicit parametrically dissipative KR-α method for real-time hybrid simulation. Earth Engr Struct Dyn 2015;44(5):735–55. https://doi.org/10.1002/eqe.2484.
[31] Chung J, Hubert GM. A time integration algorithm for structural dynamics with improved numerical dissipation: the generalized-α method. ASME J Appl Mech 1993;60(371):375.
[32] Kolay C, Ricles J. Force-based frame element implementation for real-time hybrid simulation using explicit direct integration algorithms. J Struct Engr 2018;144(2):04017191. https://doi.org/10.1061/(ASCE)ST.1943-541X.0001944.
[33] Chiou B, Darragh R, Gregor N, Silva W. NGA project strong-motion database. Earth Spect 2008;24(1):23–44. https://doi.org/10.1193/1.2894831.
[34] Kolay C. Parametrically dissipative explicit direct integration algorithms for computational and experimental structural dynamics. Ph.D. Dissertation, Department of Civil and Environmental Engineering, Lehigh University, Bethlehem, PA; 2016.
[35] Simiu E, Scanlan R. Winds Effects on Structures: Fundamentals and Applications to Design. 3rd ed. New York: John Wiley & Sons, Inc; 1996.
[36] Ricles, J., Kolay C., Marullo T. HyCoM-3D: A program for 3D multi-hazard nonlinear analysis and real-time hybrid simulation of civil infrastructure systems. Bethlehem (PA): ATLSS Engineering Research Center, Lehigh University; 2020. Report No.; 20–02.
[37] Menegotto M., Pinto E. Method of analysis for cyclically loaded RC plane frames including changes in geometry and non-elastic behavior of elements under combined normal. Proceedings of IABSE symposium on Resistance and Ultimate Deformability of Structures Acted on by Well Defined Repeated Loads; 1973; Lisbon, Portugal.
[38] Filippou F., Popov E., Bertero V. Effect of bond deterioration on hysteretic behavior of reinforced concrete joints. Earthquake Engineering Research Center, University of California, Berkeley, California. 1983 August. Report No.; UCB/EERC-83/19.
[39] Chopra A, McKenna F. Modeling viscous damping in nonlinear response history analysis of buildings for earthquake excitation. Earth Engr Struct Dyn 2016;45(2):193–211. https://doi.org/10.1002/eqe.2622.
[40] Qian X, Chopra A, McKenna F. Modeling viscous damping in nonlinear response history analysis of steel moment-frame buildings: Design-plus ground motions. Earth Engr Struct Dyn 2021;50(3):903–15. https://doi.org/10.1002/eqe.3358.
[41] Craig Jr R, Bampton M. Coupling of substructures for dynamic analyses. AIAA J 1968;6(7):1313–9. https://doi.org/10.2514/3.4741.
[42] Al-Subaihawi S. Real-time hybrid simulation of complex structural systems subjected to multi-natural hazards. Ph.D. Dissertation, Department of Civil and Environmental Engineering, Lehigh University, Bethlehem, PA; 2023.
[43] Wan E., Van Der Merwe R. The unscented Kalman filter for nonlinear estimation. In Proceedings of the IEEE 2000 Adaptive Systems for Signal Processing, Communications, and Control Symposium; 2000 October 1–4; Lake Louise, Alberta, Canada. DOI:10.1109/ASSPCC.2000.882463.
[44] Wang T., Wu B. Real-time hybrid testing with constrained unscented Kalman filter. In 5th International Conference on Advances in Experimental Structural Engineering; 2013 November 8–9; Taipei, Taiwan.
[45] Qi J, Sun K, Wang J, Liu H. Dynamic state estimation for multi-machine power system by unscented Kalman filter with enhanced numerical stability. IEEE Trans smart Grid 2018;9(2):1184–96. https://doi.org/10.1109/TSG.2016.2580584.

[46] Mandela R, Kuppuraj V, Rengaswamy R, Narasimhan S. Constrained unscented recursive estimator for nonlinear dynamic systems. J Process Crtl 2012;22(4): 718–28. https://doi.org/10.1016/j.jprocont.2012.02.001.
[47] Kolås S, Foss B, Schei T. Constrained nonlinear state estimation based on the UKF approach. Comput Chem Eng 2009;33(8):1386–401.
[48] Eberhart, R. & Kennedy, J., 1995. Particle swarm optimization. Perth, Australia, s. n., pp. 1942–1948.
[49] Wan, E. & van der Merwe, R., 2000. The unscented Kalman filter for nonlinear estimation. s.l., s.n., pp. 153–158.
[50] Higham N. Computing a nearest symmetric positive semidefinite matrix. , pp. 103 Linear Algebra its Appl 1988:103–18. https://doi.org/10.1016/0024-3795(88)90223-6.
[51] Benoit C. Note on a method for solving normal equations coming from the application of the least squares method to a system of linear equations in number less than that of the unknowns (Commander Cholesky's method). Geod Bull 1924;2 (1):67–77 (pp.).
[52] The MathWorks Inc. MATLAB [computer program]. Version: 9.13.0 (R2022b). Natick (MA), 2022.
[53] Chopra A. Dynamics of structures: theory and applications to earthquake engineering. 3rd ed. Upper Saddle River (NJ): Prentice Hall Inc; 2007.